



National Library
of Canada

Acquisitions and
Bibliographic Services Branch

395 Wellington Street
Ottawa, Ontario
K1A 0N4

Bibliothèque nationale
du Canada

Direction des acquisitions et
des services bibliographiques

395, rue Wellington
Ottawa (Ontario)
K1A 0N4

Your file Votre référence

Our file Notre référence

The author has granted an irrevocable non-exclusive licence allowing the National Library of Canada to reproduce, loan, distribute or sell copies of his/her thesis by any means and in any form or format, making this thesis available to interested persons.

L'auteur a accordé une licence irrévocable et non exclusive permettant à la Bibliothèque nationale du Canada de reproduire, prêter, distribuer ou vendre des copies de sa thèse de quelque manière et sous quelque forme que ce soit pour mettre des exemplaires de cette thèse à la disposition des personnes intéressées.

The author retains ownership of the copyright in his/her thesis. Neither the thesis nor substantial extracts from it may be printed or otherwise reproduced without his/her permission.

L'auteur conserve la propriété du droit d'auteur qui protège sa thèse. Ni la thèse ni des extraits substantiels de celle-ci ne doivent être imprimés ou autrement reproduits sans son autorisation.

ISBN 0-612-16482-9

Canada

Name Michael P. Casey

Dissertation Abstracts International is arranged by broad, general subject categories. Please select the one subject which most nearly describes the content of your dissertation. Enter the corresponding four-digit code in the spaces provided.

Physical Sciences, Pure Sciences, Physics, Astronomy & Astrophysics

SUBJECT TERM

0606

SUBJECT CODE

U·M·I

Subject Categories

THE HUMANITIES AND SOCIAL SCIENCES

COMMUNICATIONS AND THE ARTS

Architecture 0729
Art History 0377
Cinema 0900
Dance 0378
Fine Arts 0357
Information Science 0723
Journalism 0391
Library Science 0399
Mass Communications 0708
Music 0413
Speech Communication 0459
Theater 0465

EDUCATION

General 0515
Administration 0514
Adult and Continuing 0516
Agricultural 0517
Art 0273
Bilingual and Multicultural 0282
Business 0688
Community College 0275
Curriculum and Instruction 0727
Early Childhood 0518
Elementary 0524
Finance 0277
Guidance and Counseling 0519
Health 0680
Higher 0745
History of 0520
Home Economics 0278
Industrial 0521
Language and Literature 0279
Mathematics 0280
Music 0522
Philosophy of 0998
Physical 0523

Psychology 0525
Reading 0535
Religious 0527
Sciences 0714
Secondary 0533
Social Sciences 0534
Sociology of 0340
Special 0529
Teacher Training 0530
Technology 0710
Tests and Measurements 0288
Vocational 0747

LANGUAGE, LITERATURE AND LINGUISTICS

Language 0679
General 0289
Ancient 0290
Linguistics 0291
Modern 0401
Literature 0294
Classical 0295
Comparative 0297
Medieval 0298
Modern 0316
African 0591
American 0305
Asian 0352
Canadian (English) 0355
Canadian (French) 0593
English 0311
Germanic 0312
Latin American 0315
Middle Eastern 0313
Romance 0314
Slavic and East European

PHILOSOPHY, RELIGION AND THEOLOGY

Philosophy 0422
Religion 0318
General 0321
Biblical Studies 0319
Clergy 0320
History of 0322
Philosophy of 0469
Theology

SOCIAL SCIENCES

American Studies 0323
Anthropology 0324
Archaeology 0326
Cultural 0327
Physical 0310
Business Administration 0272
General 0770
Accounting 0454
Banking 0338
Management 0385
Marketing 0501
Canadian Studies 0503
Economics 0505
General 0508
Agricultural 0509
Commerce-Business 0510
Finance 0511
History 0358
Labor 0366
Theory 0351
Folklore 0578
Geography 0366
Gerontology 0351
History 0578
General

Ancient 0579
Medieval 0581
Modern 0328
Black 0331
African 0332
Asia, Australia and Oceania 0334
Canadian 0335
European 0336
Latin American 0333
Middle Eastern 0337
United States 0585
History of Science 0398
Law 0615
Political Science 0616
General 0617
International Law and Relations 0814
Public Administration 0452
Recreation 0626
Social Work 0627
Sociology 0938
General 0631
Criminology and Penology 0628
Demography 0629
Ethnic and Racial Studies 0630
Individual and Family Studies 0700
Industrial and Labor Relations 0344
Public and Social Welfare 0709
Social Structure and Development 0999
Theory and Methods 0453
Transportation 0999
Urban and Regional Planning 0453
Women's Studies

THE SCIENCES AND ENGINEERING

BIOLOGICAL SCIENCES

Agriculture 0473
General 0285
Agronomy 0475
Animal Culture and Nutrition 0476
Animal Pathology 0359
Food Science and Technology 0478
Forestry and Wildlife 0479
Plant Culture 0480
Plant Pathology 0817
Plant Physiology 0777
Range Management 0746
Wood Technology 0306
Biology 0287
General 0308
Anatomy 0309
Biostatistics 0379
Botany 0329
Cell 0353
Ecology 0369
Entomology 0793
Genetics 0410
Limnology 0307
Microbiology 0317
Molecular 0416
Neuroscience 0433
Oceanography 0821
Physiology 0778
Radiation 0472
Veterinary Science 0786
Zoology 0760
Biophysics 0425
General 0996
Medical

EARTH SCIENCES

Biogeochemistry 0425
Geochemistry 0996

Geodesy 0370
Geology 0372
Geophysics 0373
Hydrology 0388
Mineralogy 0411
Paleobotany 0345
Paleocology 0426
Paleontology 0418
Paleozoology 0985
Palynology 0427
Physical Geography 0368
Physical Oceanography 0415

HEALTH AND ENVIRONMENTAL SCIENCES

Environmental Sciences 0768
Health Sciences 0566
General 0300
Audiology 0992
Chemotherapy 0567
Dentistry 0350
Education 0769
Hospital Management 0758
Human Development 0982
Immunology 0564
Medicine and Surgery 0347
Mental Health 0569
Nursing 0570
Nutrition 0380
Obstetrics and Gynecology 0354
Occupational Health and Therapy 0381
Ophthalmology 0571
Pathology 0419
Pharmacology 0572
Pharmacy 0382
Physical Therapy 0573
Public Health 0574
Radiology 0575
Recreation

Speech Pathology 0460
Toxicology 0383
Home Economics 0386

PHYSICAL SCIENCES

Pure Sciences 0485
Chemistry 0749
General 0486
Agricultural 0487
Analytical 0488
Biochemistry 0738
Inorganic 0490
Nuclear 0491
Organic 0494
Pharmaceutical 0495
Physical 0754
Polymer 0405
Radiation 0605
Mathematics 0986
Physics 0606
General 0608
Acoustics 0748
Astronomy and Astrophysics 0607
Electronics and Electricity 0798
Elementary Particles and High Energy 0759
Fluid and Plasma 0609
Molecular 0610
Nuclear 0752
Optics 0756
Radiation 0611
Solid State 0463
Statistics 0346
Applied Sciences 0984
Applied Mechanics 0346
Computer Science

Engineering 0537
General 0538
Aerospace 0539
Agricultural 0540
Automotive 0541
Biomedical 0542
Chemical 0543
Civil 0544
Electronics and Electrical 0348
Heat and Thermodynamics 0545
Hydraulic 0546
Industrial 0547
Marine 0794
Materials Science 0548
Mechanical 0743
Metallurgy 0551
Mining 0552
Nuclear 0549
Packaging 0765
Petroleum 0554
Sanitary and Municipal 0790
System Science 0428
Geotechnology 0796
Operations Research 0798
Plastics Technology 0799
Textile Technology

PSYCHOLOGY

General 0621
Behavioral 0384
Clinical 0622
Developmental 0620
Experimental 0623
Industrial 0624
Personality 0625
Physiological 0989
Psychobiology 0349
Psychometrics 0632
Social 0451



Contents

List of Figures	v
List of Tables	vii
Acknowledgements	viii
Abstract	x
1 Introduction	1
1.1 M87 Properties	1
1.1.1 Atmosphere	2
1.1.2 Lobes and jet	6
1.1.3 Core region, VLBI-jet and accretion disk	9
1.2 Previous work	11
1.2.1 Jets—General Properties	11
1.2.2 M87 specific work	13
1.3 Simulating the M87 jet	14
2 Boundary conditions and physical constraints	17
2.1 Computer Code	17
2.1.1 ZEUS-3D	17
2.1.2 System of units	18
2.2 The atmosphere	20

2.3	The M87 jet: an analytical approach	23
2.3.1	Initial conditions and parameters	23
2.3.2	Initialization of the simulation	25
2.3.3	Results and methods of analysis	27
3	The search for the M87 jet parameters.	35
3.1	Method of Search	35
3.1.1	Selection of jet parameters	35
3.1.2	Analysis of trends: opening angle	38
3.1.3	Analysis of trends: Recollimation point	44
3.1.4	Final identification of parameters describing M87	48
3.2	The M87 jet: high-resolution simulation	51
3.2.1	Initialization	51
3.2.2	Results: opening angle	53
3.2.3	Results: recollimation point	54
3.2.4	Results: Overall jet morphology	57
4	Summary and Conclusions	65
4.1	Jet morphology	65
4.2	Opening angle	68
4.3	Recollimation point	69
4.4	General Comments	70

References	72
-------------------	-----------

Curriculum Vitae	77
-------------------------	-----------

Certificate of Examination

Saint Mary's University
Department of Astronomy and Physics

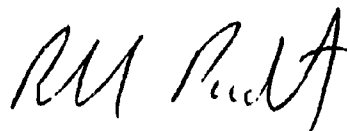


Dr. David A. Clarke
Associate Professor
Department of Astronomy and Physics
Saint Mary's University
(Supervisor)



Dr. Malcolm N. Bulter
Associate Professor
Department of Astronomy and Physics
Saint Mary's University

Dr. Ralph E. Pudritz
Professor
Department of Physics and Astronomy
McMaster University
(External Reader)



Dr. David G. Turner
Professor
Department of Astronomy and Physics
Saint Mary's University

List of Figures

1	The profiles of T94A case g	5
2	Grey-scale 2 cm VLA image of the M87 jet.	7
3	The computational grid used for the simulation of the atmosphere.	21
4	Comparison between $t = 0$ and $t = 100$ for atmosphere.	22
5	The computational grid used for LR simulations.	26
6	Determination of the half-opening angle of a jet.	28
7	Determination of the recollimation point of a jet.	30
8	Determination of stability of r_{min} with respect to time	31
9	Initial conditions of simulated jets in p - ρ space	36
10	Grey-scale pressure image of Jet 10	36
11	Contours of density and pressure, and interpolation to various θ_o . The contour values are labelled on the plots.	39
12	Contours of r_c and θ_o plotted in ρ - p space. The straight lines indicate that power laws govern the relationships.	40
13	Demonstration of the failure of the Mach angle equation.	42
14	Density and pressure as a function of azimuthal angle for Jet 10	43
15	Determination of r_c of Jet 10 at $t = 30$	44
16	Contours of density and pressure, and interpolation to $r_c = 500, 691$ (knot A), 1000, and 1400 r_j . The contours values are labelled on the plots.	47
17	The determination of the steady-state results for the candidate jet.	50

18	The computational grid used for the HR simulation.	52
19	Evolution of θ_o in HR calculation.	53
20	Evolution of r_{min} in HR calculation.	54
21	Determination of r_c for HR simulation at $t = 30$	56
22	Physical profiles of the HR jet at $t = 15$ and $t = 30$	58
23	Velocity profile along the HR jet axis at $t = 30$	59
24	Grey-scale images of pressure and density and velocity divergence < 0 of the jet.	60

List of Tables

1	The parameters of the fit from T94A case g	4
2	Conversion factors between scaled and real units	19
3	Assumed conditions of the atmosphere and jet for the analytical model . . .	25
4	Simulated jets—initial conditions and key results.	37
5	Listing of power law indices, δ , found for the r_c contours of Figure 12. . . .	48
6	The initial conditions and results for the M87 candidate jet (low-resolution) simulation.	51

Acknowledgements

First and foremost I would like to express my gratitude to Dr. David Clarke for all of the advice and guidance throughout these past two years. Without his patience throughout all those debug sessions this project would not have been possible. I would also like to thank him for reminding me of my dislike of FORTRAN! Now, if I can only convince him to learn 'C'... (Sorry Dave, couldn't resist!).

I would also like to thank Dr. David Turner, and Dr. Malcolm Butler for serving on my examination committee, and Dr. Ralph Pudritz for acting as external reader. Phil Liardee should be mentioned for advice, originally directed to David Clarke, which was instrumental in getting this project off the ground. Frazer Owen is also thanked for permission to include his VLA image of the M87 jet in this thesis.

Thanks also to Glen Petitpas who did some of the initial coding oh so long ago. Glen: remember this line?

M87ATM :The Thunderbirds Are Go !!! (F.A.B.!)

It's still printed every time the M87 code is run. How's that for a legacy!

It's been a remarkable two years, and it would not have been the same without the mutual friendship and support of my fellow graduate students:

Bev Miskolczi and Stefan Elieff: I will always remember the day the three of us met, and my amazement at finding two other people who shared my interest in aircraft. Remember when we actually had *time* to do things like go to the air show together? Stefan: I don't think I ever did thank you for finding that rather small fencing advertisement last Fall. I

can think of few better ways I could have blown off steam this past year than by poking people with swords! Quite therapeutic. Plus the other friends we've made because of it. I can't thank you enough...

Gary Gidney: When I get to Toronto, I don't think you know how much I'll miss those nights of card playing, conversation, and red wine that you and Susan could provide. It rivaled fencing for stress relief, and is not quite as tiring—although I did end up with a headache once or twice the next morning.

Mel Blake and Steve Short: All you need to liven things up in a place is to add a couple of Newfs. Always good for an outrageous story or two.

Kevin Douglas: Thanks to your CD collection, I've discovered new music I didn't know existed. And this Discman you sold me had saved my sanity countless times during the writing of this thesis.

Todd Fuller: Do you think we'll ever be able to recreate the Great Comet Hyakutake Car Stuffing Event? I think my feet are still numb! But it was a memorable moment nonetheless, like so many other times.

Wayne Barkhouse: Looks like we'll be seeing even more of one another in Toronto. I'm glad there will be somebody there I know. I'll thank you in full when our Ph.D theses are done!

Abstract

Observations of the jet in M87 and its surroundings are used to constrain hydrodynamical calculations of this object. These constraints include atmospheric profiles of the gas surrounding M87, the observed point of recollimation at Knot A, the observed half-opening angle of the jet ($\sim 3^\circ$ before deprojection), the inferred inclination of the jet with respect to the plane of the sky ($\sim 42^\circ$), *etc.* Many jets are simulated in a systematic search for the parameters which reproduce the opening angle and recollimation point of the M87 jet. From those, estimates are made of the density and pressure of the M87 jet, and of such quantities as mass flux, and power output. During this search it was also found that the simulated jets did not obey the Mach angle relationship, and that recollimation of a jet depends primarily on the ram pressure of a jet as opposed to the thermal pressure.

1 Introduction

The jet in M87 (NGC 4486, Virgo A, 3C 274) in the Virgo cluster is one of the closest examples of an extragalactic jet [15 Mpc; only Centaurus A (NGC 5128) is closer; Hesser *et al.* 1984] and has thus provided astronomers with a tremendous opportunity for close observation. This means better models of the radio source associated with M87 can be constructed and tested with greater confidence than for objects further away. It is the purpose of this thesis to present numerical simulations of the M87 jet and atmosphere which provide insight into the physical properties (*e.g.* density and pressure) of the jet.

1.1 M87 Properties

An excellent review of the basic properties of the jet and surroundings of M87 can be found in Biretta (1994). Some of the major points will be reviewed here, and certain relevant features will be explored in greater detail. Specifically, the surrounding atmosphere, jet, radio lobes, and galactic core region will be reviewed, as these are the most relevant to this work.

M87 is one of two large dominant elliptical (E0/1) galaxies residing in the Virgo cluster. M87 and its jet have been observed at frequencies ranging from radio waves to gamma rays, at scales from 0.01 pc to greater than 50 kpc. The total information from all of these observations is quite staggering, and is best presented by breaking the M87 system up into its various components.

1.1.1 Atmosphere

M87 is at the centre of a large cooling flow comprised of hot gas which radiates copiously in the x-ray regime (Lea, Mushotzky, & Holt 1982, Canizares *et al.* 1982, Fabricant & Gorenstein 1983, hereafter FG, Stewart *et al.* 1984). In two papers, Tsai (1994a; 1994b; hereafter T94a and T94b) makes a detailed reanalysis of data from the *Einstein Observatory* Image Proportional Counter (IPC), High Resolution Imager (HRI), Focal Point Crystal Spectrometer (FPCS) and the Solid State Spectrometer (SSS).

In T94a spherically symmetric electron density profiles of the form

$$n_e(r) = n_0 \frac{(r/a_1)^{-\alpha_1}}{1 + (r/a_1)} \quad (1)$$

and temperature profiles of the form

$$T(r) = T_\infty \left(\frac{r}{a_2 + r} \right)^{\alpha_2} \quad (2)$$

originally from Bertchinger & Meiksin (1986) were fit to the HRI and IPC surface brightness profiles. Here, r is the distance in parsecs from the core (see Figure 1 for a sample fit).

Tucker and Rosner (1983; hereafter TR) from HRI and IPC data point out that the density profile is consistent with a power law at small radii ($n \propto r^{-1.1}$), and a different power law at large radii, but with a somewhat larger negative slope ($n \propto r^{-1.3}$). Note equation (1) has this property, $n_e \propto r^{-\alpha_1}$ at small radii, and $n_e \propto r^{-\alpha_1-1}$ at large radii, although the difference between the two power law indices is greater than in TR. Previously it has been determined that $\alpha_1 = 0.36$ (FG), so Tsai fixes α_1 to this value for most fits, including the fit used in this project (his case g). Both a_1 and n_0 are additional parameters

of the fits. The position of the “break” between the two power laws is given by a_1 , and the density scale of the system by n_0 . (Note when $r = a_1$, $n_e = n_0/2$.)

FG has observed that at radii greater than $\sim 6'$, IPC spectral observations show the temperature to be roughly constant. Lea *et al.* (1982) find this value to be 3.8×10^7 K. However at small radii, TR suggest the temperature profile is consistent with a rising power law based upon observations of low-temperature gas by the SSS (Lea *et al.* 1982), and the FPCS (Canizares *et al.* 1982). The temperature profile given by equation (2) satisfies both these behaviours. It gives a power law at small radii (index given by α_1), and asymptotically approaches a constant temperature ($T_\infty = 3.8 \times 10^7$ K). The “break” between these two behaviours occurs roughly at $r = a_2$. Both a_2 and α_2 are free parameters of the fit.

Fits to equations (1) and (2) enabled Tsai to make predictions of the widths of the 7 keV Fe K Line and compare them to FPCS data. Theoretical spectra were also constructed and compared to spectra measured by the SSS. In fitting these spectra, oxygen abundance, [O], was also a free parameter.

T94a also considers the effects of varying such factors as the element abundances in the system (*e.g.* [Fe]), the assumed gas column density, N_H , to M87, differences in assumed atomic emissivities, and the choice of density profile. Cases were also considered in which T_∞ was changed (to 2.2×10^7 K) in order to reflect the large uncertainties associated with the experimental determination of this quantity (the effects on the fits were found to be small.)

T94b perform similar fits in the context of a multiphase medium, in contrast to T94a

Table 1: The parameters of the fit from T94A case *g*.

a_1 (kpc)	α_1	$n_0(10^{-2}\text{cm}^{-3})$	a_2 (kpc)	α_2	$T_\infty (10^7 \text{ K})$
7.95	0.36	4.87	38.7	0.491	3.8

which assumes a single medium. T94b determined that if constraints from x-ray data were considered only, then fits to a multiphase medium [in which a component of the cooling flow cools, and drops out of the flow (White & Sarazin, 1990)] gave mass dropout rates of zero, and essentially recovered the fits of T94a. However, if the optical mass determinations of Sargent *et al.* (1978) were included, multiphase models were required to fit the data.

For calculating the atmosphere surrounding M87, this project uses the parameters found in case *g* of T94a (single phase), as it is this case that provides the best fit to the data presented in his paper. The best-fit model parameters are shown in Table 1. This case also assumes an $[\text{Fe}] = 0.5$ abundance with respect to solar values, column density of hydrogen, $N_H = 3.18 \times 10^{21}\text{cm}^{-2}$, and fits an oxygen abundance of $[\text{O}] = 2.38$ with respect to solar values. Figure 1 shows plots of the profiles using the parameters of Table 1.

Note that simulations of the jet will concern mainly the inner few kiloparsecs of the atmosphere. This means that the simulated jets will fall within the steadily increasing part of the temperature curve, well away from the asymptotic region. As for the electron number density, the kink between the two power laws occurs at ~ 8 kpc, so work will be mainly in the region described by the “inner” power law.

One other crucial assumption is made with respect to the atmosphere. It is assumed

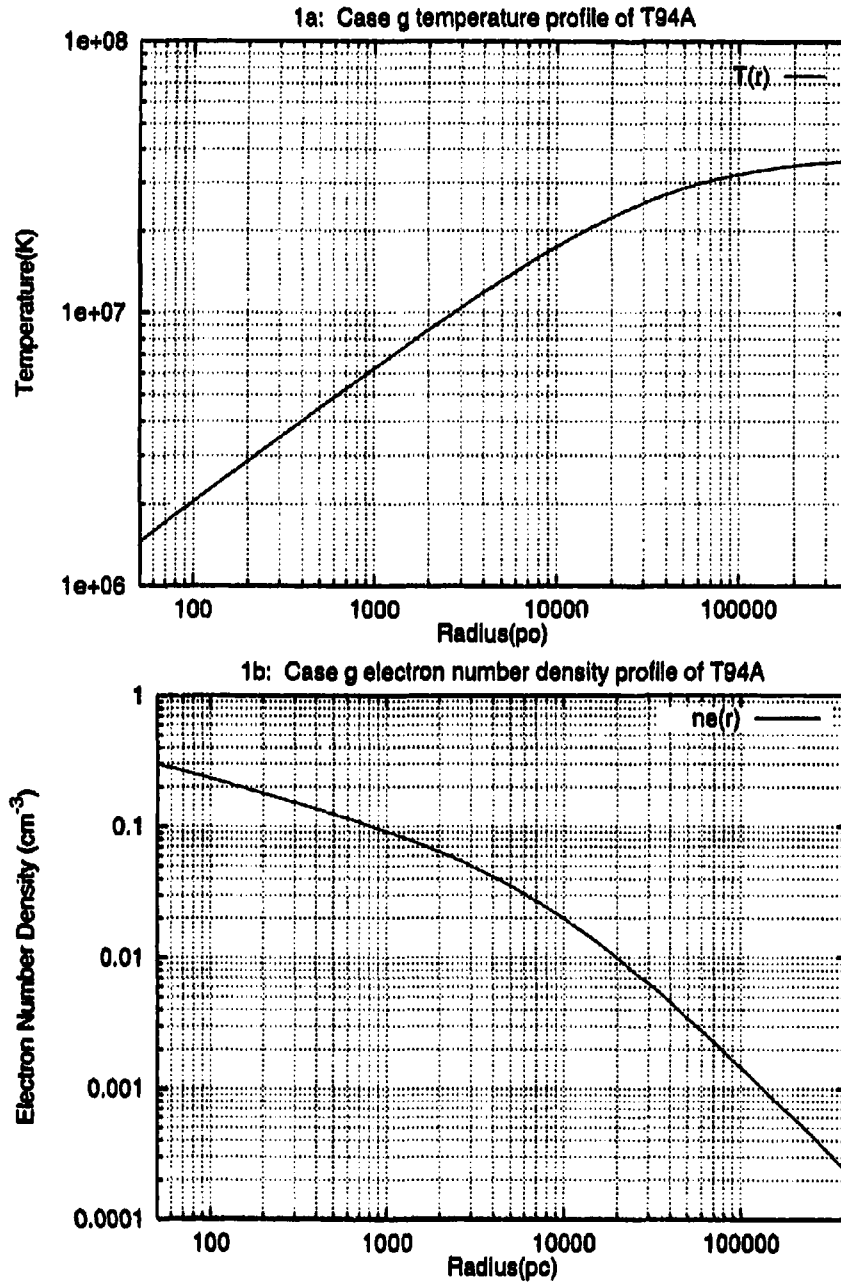


Figure 1: The profiles of T94A case *g*.

the atmosphere is neutral, and is comprised of electrons and protons. Thus equation (1) also describes the proton number density, n_p as a function of radius, and at any point the density, ρ , would be given by

$$\rho = m_p n_p + m_e n_e = m_p n_e + m_e n_e = n_e (m_p + m_e) \quad (3)$$

where m_e and m_p are the mass of the electron and proton respectively.

1.1.2 Lobes and jet

One of the most distinguishing features of the M87 system is an ~ 2 kpc long jet. It is interesting to note that this was also the first extragalactic jet ever discovered, originally observed by Curtis (1918).

Because the jet has a remarkably similar morphology at both optical and radio wavelengths (Turland 1975; Owen, Hardee and Cornwell, 1989, hereafter OHC89; Ford *et al.* 1994) these regimes provide the best clues to the morphology of the jet. The jet is comprised of a series of “knots” (Figure 1.1.2), areas of emission so named because they were unresolved in the original radio images (Turland 1975). [The classical designations of Neito and Lelievre (1982) for the various knots are used: A to I in terms of decreasing radio intensity.] Despite the existence of knots along the length of the jet, further evidence suggests that the inner jet is a continuous cone (OHC89). It is found that from the core to knot A (a projected distance of ~ 1 kpc, hereafter referred to as the inner jet), the jet is distinctly conical with an apparent opening angle of $6^\circ 0'$ full width quarter maximum (FWQM) (not corrected for projection effects) from a 15 GHz VLA image at $0''.1$ resolution



Figure 2: Grey-scale 2 cm VLA image of the M87 jet. The labels indicate the position of the knots. From Owen, Hardee & Cornwell (1989). Courtesy of Frazer Owen.

(OHC89). This image also indicates that emission seems to be mainly from the surface as evidenced by the edge-brightened morphology of the jet over most of its length. Filamentary structures also seem to be wrapped around the surface of the inner jet.

Beyond knot B the jet seems to undergo numerous changes in direction, and appears to move from side-to-side quite violently. This is evident from long-term proper motion studies of the jet by Biretta, Zhou, and Owen (1995), who are careful to point out that whether the inferred velocities imply bulk motion, and/or phase effects remains uncertain. The end result is that we adopt a velocity of $0.3c$ as a *lower limit* (Biretta 1994). This is also approximately the apparent velocity measured by Reid *et al.* (1989) using the VLBI for the nuclear jet region (*i.e.* close to the core). The edge-brightened features and filamentary structures continue after knot A, but after this point, continuing to knot B, the jet has a

distinctly cylindrical shape. Evidently something has caused the jet to recollimate. The cause of the recollimation is one of the issues addressed in this work.

The jet eventually ends in a tail, dissipating gradually into a large radio lobe. The radio lobe is presumably the result of the jet ploughing into the surrounding atmosphere and inflating a large cavity ~ 3 kpc in extent (Hines, Owen, & Eilek, 1989). The total radio source is ~ 5 kpc in extent because there are actually *two* radio lobes (but only one obvious jet), leading to speculation that there is, in fact, a second unseen counter-jet. Evidence for a counter-jet has slowly been increasing over the past five years, including such discoveries as the optical (Stiavelli *et al.* 1992; Sparks *et al.* 1992), and infrared (Neumann *et al.* 1995) counterparts to the eastern lobe of M87, particularly a region resembling a hot spot.

The radio lobes themselves dominate Virgo A. The radio source is classified as a Fanaroff-Riley type I (FR-I) source (Fanaroff & Riley 1974) because of its relatively low power output ($P_{178MHz} \sim 1 \times 10^{25} \text{ W Hz}^{-1}$). However, the one-sided nature of the jet is more characteristic of an FR-II source. Fanaroff & Riley (1974) found a correlation between jet-sidedness, and power output. Specifically, higher-powered radio sources ($> P_{178MHz} \sim 3 \times 10^{25} \text{ W Hz}^{-1}$, FR-II sources) tend to have one-sided jets, while lower-powered radio sources ($< P_{178MHz} \sim 3 \times 10^{25} \text{ W Hz}^{-1}$, FR-I sources) tend to have counter jets. Note that the one-sided nature of M87 makes it one of several known exceptions to this rule (*e.g.* Centaurus A is also a one-sided FR-I source; Clarke, Burns & Norman 1992), a fact that could be related to its intensity lying so close to the dividing line between the two classifications of radio sources (Biretta 1994).

The mechanism for emission from the jet and lobes is most consistent with synchrotron radiation and can account for observations ranging from the radio to x-ray regimes (Biretta, Stern & Harris 1991). In fact, it is the continuous synchrotron emission spectrum that has made determining the bulk velocity of the material in the jet so difficult. No spectral lines are present in the data, and therefore velocities from Doppler shifts cannot be determined.

The actual composition of the jet (and for most other extragalactic jets) is thought to be free electrons and protons (*e.g.* Celotti & Fabian 1993). However electron-positron jets have also been considered and cannot be ruled out (*e.g.* Ghisellini *et al.* 1992; Reynolds *et al.* 1996). Note that in this project the former is assumed, and thus electron and proton number densities relate directly to density as in equation (3).

1.1.3 Core region, VLBI-jet and accretion disk

It is also informative to look at the core regions of the system. On smaller scales, 18 cm VLBI images of Reid *et al.* (1989) show a jet opening angle of $\sim 10^\circ$ at distances of about 20 pc from the core. Milliarcsecond observations of the nucleus suggest that the material in the jet must collimate within 1 pc of the central engine, on a size scale less than 0.01 pc (Spencer and Junor, 1986). These small scales suggest that the central engine for the jet is a super massive black hole (SMBH) fed by an accretion disk.

It is rather remarkable to note that an accretion disk *has* actually been observed (Jarvis & Peletier 1991). Furthermore HST data of the accretion disk (Ford *et al.* 1994, Harms *et al.* 1994) suggest a mass of $(2.4 \pm 0.7) \times 10^9 M_\odot$ for the SMBH by assuming Keplerian motion of matter about the central object. Spiral structure is also observed in the disk,

with two or more arms reminiscent of those in spiral galaxies wrapping around the outer regions. With this in mind, Chakrabarti (1995) did a similar fit to the HST data as that of Harms *et al.* (1994) but included spiral shock waves in his calculations and found a slightly higher mass of $4 \times 10^9 M_{\odot}$.

Regardless of the exact value of the central mass, it is interesting to note that M87 provides some of the most conclusive evidence for the existence of a SMBH at the centre of *any* galaxy. It also provides some of the best evidence that extragalactic jet production is linked to large black holes.

Kinemematical studies of the accretion disk have proved useful for another reason; they provide an estimate for the inclination of the disk to the plane of the sky. Ford *et al.* (1994) estimate an inclination of $42^{\circ} \pm 5^{\circ}$. Biretta (1994) also estimates from a variety of considerations that the inclination of the jet to the line of sight is $\sim 40^{\circ}$. If the jet is approximately perpendicular to the accretion disk, as is expected from most models of jet formation, then these two values are in good agreement. For this work, an inclination angle of 42° for the jet with respect to the line of sight has been chosen. Thus, deprojection of the 6° opening angle according to the geometry described by Oppenheimer & Biretta (1994) implies an actual opening angle of $\sim 4.4^{\circ}$.

1.2 Previous work

1.2.1 Jets—General Properties

Many computer simulations have been performed with the goal of understanding the underlying physics and classifying jet morphologies according to initial conditions (Norman, Winkler, & Smarr 1983; Norman, Smarr & Winkler 1985; Clarke, Norman & Burns 1986; Hardee & Norman 1988, 1990; Lind *et al.* 1989; Hardee *et al.* 1991, 1992, 1995; Appl & Camenzind 1992; Loken *et al.* 1993; Clarke 1996b). Within this body of work are two-dimensional (2D) and three-dimensional (3D) simulations of jets with various initial values of density, pressure, velocity and magnetic field strength propagating into a variety of atmospheres. Through such work and the vast amount of radio observations of such objects (*e.g.* Hardee, Bridle, & Zensus 1996), the general properties of jets and their effects on their environs are fairly well understood.

For example, simulations have shown that overpressured jets (internal pressure of the jet, p_j , greater than the pressure of the ambient medium, p_a) expand until pressure equilibrium is reached between the two materials (Norman, Winkler, & Smarr 1993). The expansion of the M87 jet to knot A therefore suggests the jet is overpressured at the core.

It is also believed that the jet is underdense (density less than that of the ambient medium), and highly supersonic (Mach number of the jet, $M_j > 5$), since numerical simulations show that only light, fast jets can produce the extended lobes observed in sources such as Virgo A (Norman, Smarr & Winkler 1985). Note that this does not mean the jet cannot be overdense at the core. As the jet expands, its density decreases and so it need

only be underdense when its leading edge encounters the atmosphere beyond knot C, and probably knot A.

The magnetic field strength in the lobes is thought to be weak (not important dynamically), as large lobes are not produced in simulations containing large magnetic fields (Clarke, Norman, & Burns 1986; Lind *et al.* 1989; Appl & Camenzind 1992). For the most part, a weak field in the lobes infers a weak field in the jet, except for certain unlikely magnetic field configurations (Clarke 1996b). Although these configurations cannot be ruled out, it will be assumed here that the M87 jet transports a weak magnetic field. If, in fact, the jet does transport a strong magnetic field, the fields could contribute to the recollimation of the jet. This project will determine whether strictly hydrodynamical calculations can recollimate the jet (*i.e.* without the use of magnetic fields).

A high Mach number for the jet is also supported by the simulations of Loken *et al.* (1993) which show that high Mach number jets may travel long distances before axial symmetry is broken (M87 is approximately axially symmetric until it reaches knot C). Furthermore, Loken *et al.* (1993) found that axial symmetry is broken via internal shocking which serves to heat the jet, thereby increasing the internal sound speed and decreasing its Mach number, eventually making it more susceptible to disruption. This may be the origin of knots B and C, and the mechanism behind the eventual disruption of the jet.

The stability of the jet against disruption may be enhanced by more than one factor. If the jet is overdense (and thus more ballistic) at its source, this may increase the distance before disruption (Norman, Winkler, & Smarr 1983). Others have shown that atmospheric

temperature and density gradients such as those modelled by T94a further stabilize a jet against disruption (Hardee *et al.* 1991, 1992; Loken *et al.* 1993). Hardee (1982, 1986, 1987a,b) has shown that jet expansion and cooling serve to slow the growth of perturbations which would otherwise disrupt the jet.

In summary, from previous general simulations it may be expected that the M87 jet may be initially overdense, overpressured, and have a high Mach number, with little magnetic field. The atmospheric profiles of T94a are consistent with a stable jet at least until knot A is reached. These considerations are fundamental to this work and will provide some of the initial conditions for the simulations presented in the following chapters.

1.2.2 M87 specific work

As the general properties of jets are understood from simulations and observations, it remains to be seen whether any particular source can be modelled successfully.

In the 1980s it was thought that the various knots of the inner jet were produced by regions of high compression along the length of the jet (Falle & Wilson 1985). Given the observations of the time, this was certainly a valid interpretation particularly since numerical calculations by Falle and Wilson (1985; 1986) reproduced the observations to a reasonable degree of accuracy. However, more recent observations suggest that the jet has more of a conical shape, with surface features dominating the observations (OHC89). This means that Falle and Wilson's model no longer matches the observations.

Also, as discussed in § 1.1.1, the *Einstein Observatory* data permit more detailed modelling of the atmosphere which Hardee, White & Norman (1993; hereafter HWN) used to

perform more representative two-dimensional hydrodynamical simulations. HWN were able to reproduce to first order the constant opening angle, followed by recollimation. However, as they mention, their atmospheric profiles did not accurately reproduce the x-ray surface brightness inside 10 kpc. This problem has since been overcome by T94a and thus the profiles described by equations (1) and (2) are more suitable for use in simulations. Further, since the HWN simulation, observations have shown that the jet is inclined significantly with respect to the plane of the sky ($\sim 42^\circ$), whereas they had assumed the jet was in (or at least close to) the plane of the sky.

Accounting for projection effects revealed by the inclination discovery changes two important jet parameters. First, the recollimation point (knot A) is further out from the centre of the system than previously believed, and therefore the conditions under which the jet recollimates are significantly different. Second, the jet is intrinsically narrower, and thus the model of HWN requires a higher initial Mach number to be consistent with a smaller true opening angle. Thus a new set of simulations are needed to help explain the M87 jet system.

1.3 Simulating the M87 jet

In this project a survey of two-dimensional computer simulations will be used to select conditions of the jet near the core which will reproduce two particular observables: the opening angle, and the recollimation point. Note that large computational requirements make it impractical to perform extensive parameter searches in 3D. Calculations will be strictly hydrodynamical, as magnetic fields are assumed to be weak and not important

dynamically. A two-fluid approach will be used, so that the jet and atmosphere can be treated as relativistic (hot) and nonrelativistic (cold) monatomic gases respectively.

For the purposes of this work the actual mechanism that launches the jet (*e.g.* see Ustyugova *et al.* 1995; Contopoulos & Lovelace 1994; Ouyed, Pudritz & Stone 1996) is not a concern. The main interest is how the jet interacts with the surrounding medium, which in itself should provide insight into the internal properties of the M87 jet (*e.g.* density and pressure, cause of recollimation, *etc.*) Thus all simulations are started at a minimum distance of 50 pc from the core of the galaxy. This choice should not affect the results significantly. As the jet enters the grid, the expansion rate of the outflow asymptotically approaches the analytically determined rate (see § 2.3). Thus, the evolution of the jet is relatively insensitive to the actual location of the inner boundary.

A significant portion of this project is devoted to developing an efficient *procedure* to identify the simulation with the appropriate opening angle and recollimation point for M87. This procedure is predicated on the assumption that systematic variations in input parameters (*e.g.* density, pressure, bulk velocity of the jet) produce systematic variations in observables (*e.g.* opening angle, recollimation point). Thus, should new observations render the specific conclusions of this project obsolete (*e.g.* different orientation of the jet with respect to the line of sight, better estimate of the outflow velocity, *etc.*) it would be a relatively easy matter to reconcile simulations with improved observations. Further, this procedure could be applied to other sources with well-defined opening angles and recollimation points (*e.g.* 3C 219; Clarke *et al.* 1992).

The state of the art has now advanced sufficiently so that detailed modelling of individual sources may be contemplated. Only with such efforts will the present understanding of radio jets be truly tested. Such modelling has already been done with the radio source Cygnus A (Clarke, Harris, Carilli 1996). In this work, detailed modelling of the radio source Virgo A will be attempted. The results of this work should provide the appropriate initial conditions for a (future) full-blown 3D calculation in which many more details of the source (and model) can be explored (*e.g.* morphology of the radio lobe, cause of disruption of the jet, *etc.*), and thus truly test our understanding of this complex source.

2 Boundary conditions and physical constraints

As in any set of coupled differential equations, hydrodynamics demands sufficient boundary and initial conditions in order for the system to have a unique solution. In this chapter the necessary conditions for performing simulations of the M87 system are given along with a sample jet calculation and the methods developed to analyze it.

2.1 Computer Code

2.1.1 ZEUS-3D

Simulations are performed using the three-dimensional magnetohydrodynamics (MHD) code, ZEUS-3D (Clarke 1996a) with modifications required to compute two co-existing fluids with different adiabatic indices (Jun, Clarke, & Norman 1994). The code utilizes a second-order accurate, monotonic, upwinded, time-centred scheme (van Leer 1977) to perform interpolations. A von Neumann-Richtmyer artificial viscosity is used to smear a shock out over several grid zones in order to stabilize it (*e.g.* Richtmyer and Morton 1967). Two dimensional calculations are performed in spherical coordinates with magnetic fields turned off (for a purely hydrodynamical calculation), for an assumed axisymmetry about the inferred rotation axis of the central SMBH. Jets are injected along the rotation axis of the system. The atmosphere is modelled as a compressible “cold” fluid with adiabatic index $\gamma_a = 5/3$ (*e.g.* thermal nonrelativistic), while jet material is modelled as a second “hot” fluid with adiabatic index $\gamma_j = 4/3$ (*e.g.* thermal relativistic). Note that ZEUS-3D is a Newtonian code. Strictly speaking only subrelativistic bulk velocities can be modelled.

2.1.2 System of units

For computational convenience, simulations have been performed using scaled, dimensionless units. Most results will be quoted in these units, unless otherwise stated. It is informative to review the process which determines conversions between these dimensionless units and standard units.

The inner boundary, r_{in} , of the 2D polar grid was chosen to be 50 pc, and serves as the fiducial point for scaling the flow variables. Thus, velocities and densities are all scaled by the sound speed and density at r_{in} . In scaled units, therefore, $c_{in} = 1$ and $\rho_{in} = n_{c_{in}}(m_p + m_e) = 1$.

The adiabatic sound speed, c_s , is given by

$$c_s^2 = \frac{\gamma p}{\rho}. \quad (4)$$

In scaled units the pressure at the inner boundary is therefore $p_{in} = 0.6$.

Temperature and pressure are related via

$$p = n_e k_b T_e + n_p k_b T_p \quad (5)$$

where T_e and T_p are the temperature of the electron and proton gasses respectively. Assuming the protons and electrons are in thermodynamic equilibrium ($T_e = T_p$) and using equation (3), equation (5) can be written as

$$p = \frac{2k_b}{m_p + m_e} \rho T. \quad (6)$$

The temperature is scaled such that $2k_b/(m_p + m_e) = 1$, and thus the temperature at the inner boundary, T_{in} , is given by $T_{in} = 0.6$.

Table 2: Conversion factors between the scaled units of ZEUS-3D and real units.

quantity	ZEUS-3D dimensionless units	M87 real units
density	1	$5.023 \times 10^{-22} \text{kg m}^{-3}$ $5.023 \times 10^{-25} \text{g cm}^{-3}$
pressure	1	$2.002 \times 10^{-11} \text{Pa}$
temperature	1	$2.415 \times 10^6 \text{K}$
velocity	1	$1.996 \times 10^5 \text{m s}^{-1}$ $2.042 \times 10^{-4} \text{pc yr}^{-1}$
time	1	$3.008 \times 10^{11} \text{s}$ $9.533 \times 10^3 \text{yr}$
mass	1	$1.088 \times 10^{29} \text{kg}$
distance	1	$6.006 \times 10^{16} \text{m}$ 1.946 pc

The unit of distance is defined as the radius of the jet (r_j) at 50 pc given a constant half-opening angle of $2^\circ 23'$. Thus $r_j = 1.95 \text{ pc}$ for the jet in M87. The characteristic unit of time, t_{ch} , is then easily computed from $t_{ch} = r_j/c_{in} = 9500 \text{ yrs}$.

The system of characteristic ZEUS units has now been completely determined. The relationships just given, along with equations (1) and (2), can be used to calculate the equivalent quantities in conventional units thus determining conversion factors between ZEUS and conventional units. This is summarized in Table 2. The first column labels the quantity, the second and third columns show the relationship between dimensionless and real units. Quantities are given in SI units, and if appropriate, units more common to astronomy.

2.2 The atmosphere

It is important to note that the atmosphere described in § 1.1.1 is an empirical “best-fit” by T94a. As such, it does not represent a physical model and nothing guarantees its stability over time. Since a steady-state atmosphere is desired, a simulation must be performed in order to determine the evolution of the atmosphere, if any, over the course of a calculation. If the evolution is small, we can assume a steady-state atmosphere without having to resort to artificial measures that enforce a strict steady-state.

To this end, a grid was initialized from 50 pc ($25.7 r_j$) to 8500 pc ($4367 r_j$) containing 150 geometrically stretched zones in the radial direction with a resolution of $0.89 r_j$ at the inner boundary, and $147 r_j$ at the outer boundary. Fifty uniform zones were spaced over 90° in the azimuthal direction, giving a resolution of 1.8 (3.14×10^{-2} radians) per zone (see Figure 3). The atmosphere was evolved to $t = 100$, which is longer than any jet calculation that was performed in the following chapters.

Figure 4 shows the results of the simulation in which the $t = 100$ profiles are overlaid on the original $t = 0$ profiles. Because of azimuthal symmetry, any changes will be in the radial direction.

Changes in density and pressure have occurred mainly in the first $\sim 200 r_j$, and are all less than 20%. Beyond $200 r_j$, all changes are insignificant. Velocities are extremely small, with $v < |0.08|$ (8% of c_{in}) at all points. Mach numbers are similarly small, never exceeding 0.028. Most jet simulations in this project were run to a maximum of $t = 30$ or $t = 45$, and so the measured effects are even less than those depicted in Figure 4. Thus, for the

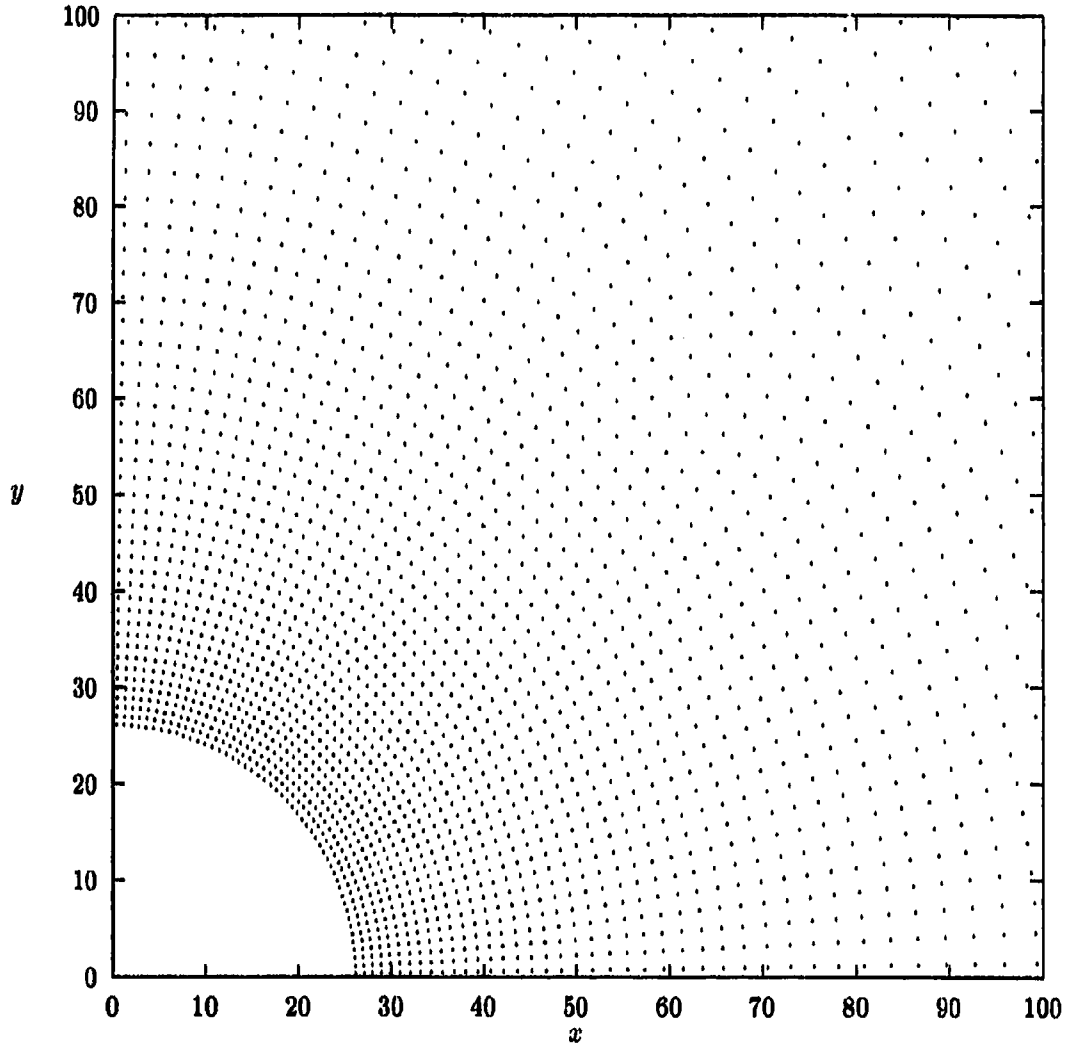


Figure 3: The inner $100 r_j$ of the grid used for simulating the atmosphere, the points marking the centre of each zone. Distances are in units of r_j . Note that the actual grid extends to $4367 r_j$ (8500 pc).

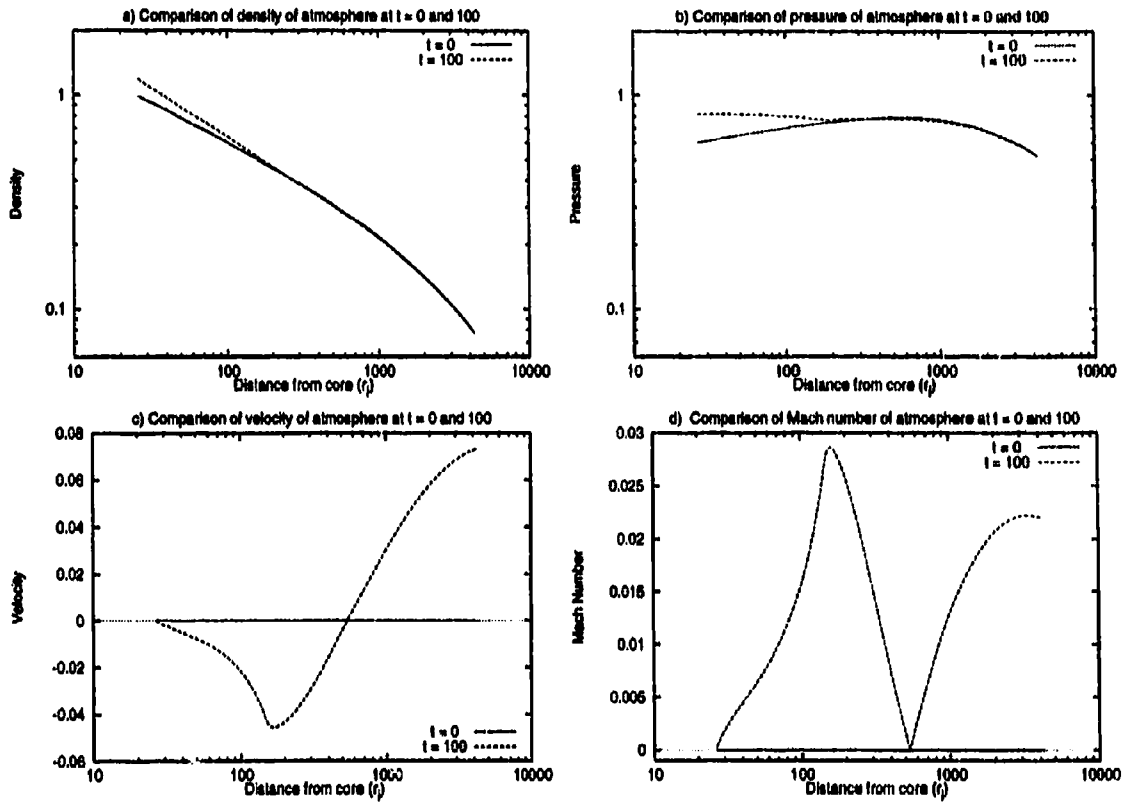


Figure 4: Comparison between $t = 0$ and $t = 100$ for atmosphere.

purposes of this work, the atmospheric profiles of T94a may be considered static.

2.3 The M87 jet: an analytical approach

Appropriate initial parameters of the jet must be selected which will reproduce the gross observations, namely the FWQM 4°4 opening angle and sudden recollimation at knot A ($\sim 691 r_j$). There are three primary initial conditions in the absence of magnetic fields that must be determined: the pressure, density, and bulk velocity at the inner boundary of the jet. From observations, if one fixes the velocity at $0.3c$, in principle the pressure and density can be constrained (if indirectly) by the opening angle and recollimation point. In other words, a unique opening angle and recollimation point pair can be determined via a unique choice of pressure and density once a velocity is chosen.

This section presents a simple analytical model for the M87 jet, and why it ultimately fails. The section also introduces the diagnostic tools necessary for evaluating the simulations in the parameter survey described in the next chapter.

2.3.1 Initial conditions and parameters

In the analytical derivation, the jet is assumed to recollimate at knot A because the thermal pressure of the jet comes into equilibrium with the thermal pressure of the ambient material. The pressure and temperature of the atmosphere at knot A is known (for the pressure indirectly) from equations (1) and (2). If constant adiabatic expansion is also assumed, in which case

$$\rho_j \propto r^{-2} \tag{7}$$

and

$$p_j \propto r^{-2\gamma}, \quad (8)$$

then from the initial calculations of the condition of the jet at knot A, properties of the jet at the inner boundary (from where the jet will be launched) can also be determined.

One might also assume that a jet with constant opening angle has the half-opening angle, θ_o , given by the Mach angle

$$\tan \theta_o = \frac{c_j}{v_j} \quad (9)$$

where c_j is the internal sound speed of the jet, and v_j is the bulk radial velocity (away from the core) of the jet. Substitution of equation (4) into equation (9) yields:

$$\rho = \frac{\gamma p}{\tan^2 \theta_o v_j^2}. \quad (10)$$

With the equation of state

$$p = (\gamma - 1)e, \quad (11)$$

equation (10) becomes

$$\rho = \frac{\gamma_j(\gamma_j - 1)e}{\tan^2 \theta_o v_j^2}. \quad (12)$$

With these assumptions we arrive at the initial parameters for a candidate model for the jet, shown in Table 3, scaled according to the discussion in § 2.1.2. Also listed are the presumed conditions of the jet and atmosphere at knot A. There are significant problems with this calculation. These will be discussed, along with the results of the corresponding simulation, in the next subsection. Whatever the problems, however, this model is based

Table 3: Initial parameters for the analytically derived jet along with the atmosphere and jet at knot A.

Position	ρ	p	e	v
Jet (50 pc)	22.0	5090	15300	450.5
Jet (knot A)	0.0297	0.782	2.35	450.5
Atmosphere (knot A)	0.263	0.782	1.17	0.00

on simple assumptions and is therefore reasonably easy to grasp and calculate. It will serve as a useful reference against which other simulations may be compared.

2.3.2 Initialization of the simulation

In order to test the validity of the values in Table 3, a 200×35 zone polar grid was initialized. The radial direction ran from 50 pc ($25.7 r_j$) to 8500 pc ($4367 r_j$), respectively, resolved by 200 geometrically expanding zones from the inner boundary outward (grid resolution $0.668 r_j$ to $110.72 r_j$), The angular direction was resolved by 35 zones, 15 zones resolving the first 1.5 angular jet radii ($3^\circ 35'$; resolution $0^\circ 223'/\text{zone}$), and 20 geometrically expanding zones resolving the region from $3^\circ 35'$ to 90° (grid resolution $0^\circ 223'$ to $18^\circ 1'$). Ten zones resolved the jet at the inner boundary with all zones having an initial velocity parallel to the jet axis. The jet was evolved to $t = 30$, although the leading edge of the jet actually left the grid at about $t = 19$. Figure 5 shows the inner $100 r_j$ of the grid used, where each dot represents the centre of a zone.

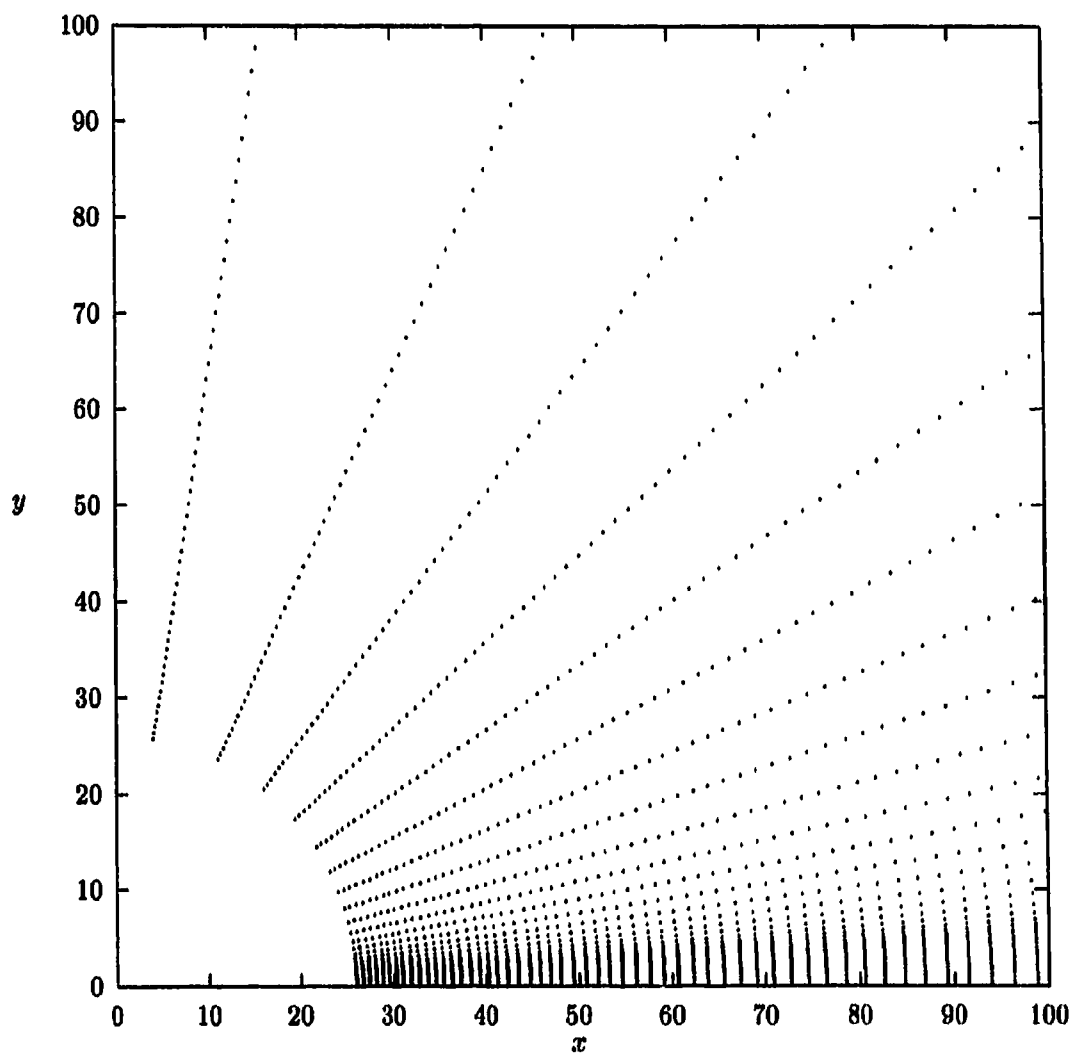


Figure 5: The inner $100 r_j$ of the grid used in most jet calculations, the points marking the centre of each zone. Note the concentration of zones along the x-axis. The jet is launched parallel to the x-axis. Distances are in units of r_j . Note the actual grid extends to $4367 r_j$ (8500 pc).

2.3.3 Results and methods of analysis

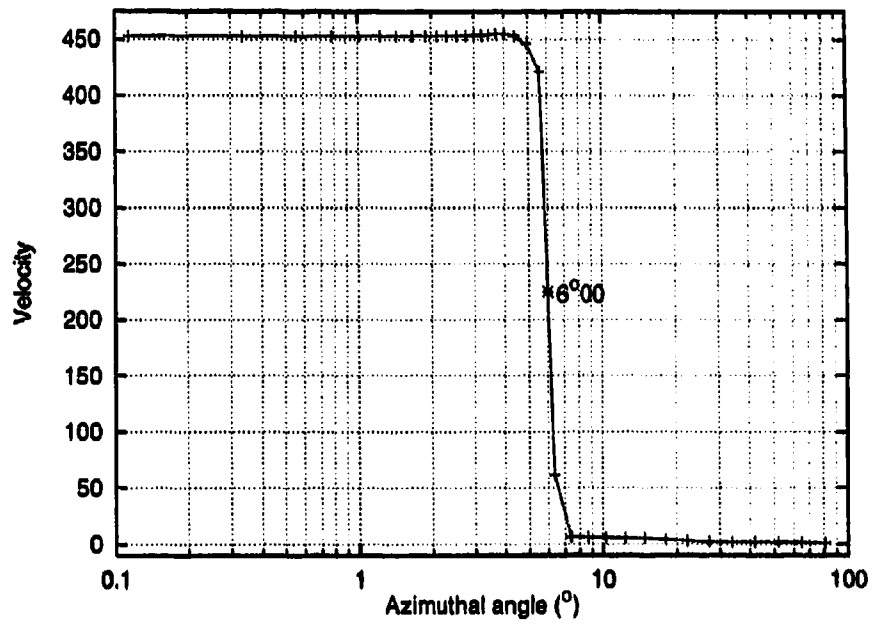
To evaluate the success of this simulation and those in the following chapter, appropriate diagnostic methods had to be developed. In particular, these methods need to identify unique and objective values for the opening angle and recollimation point of a computer-generated jet.

Figure 6a shows a 1D slice through the jet at constant radius $r = 145.4 r_j$ of v_1 (the radial component of the velocity) plotted against azimuthal angle. The edge of the jet is well defined by this profile, as velocity drops quite dramatically in a small number of zones from the initial flow velocity to almost zero. The half-opening angle, θ_o , is defined here as the angle at which the velocity drops to $v_1 = 225$ (approximately half the initial flow velocity). An interpolation is performed to $v_1 = 225$ to find the appropriate angle corresponding to this velocity.

Note for this jet, $\theta_o = 6^\circ 00$ at the particular epoch of the calculation chosen. Herein lies a possible problem in the ability to measure a unique value for θ_o . Figure 6b shows a plot of θ_o at $r = 145 r_j$ plotted against time, in which it is obvious θ_o evolves with time before reaching a steady-state. In general, measuring θ_o before steady-state is reached leads to an underestimate of the final opening angle.

There is nothing particularly special about the distance $r = 145.4 r_j$ either. Figure 7 shows various visual representations of the jet shape. Figure 7a is a grey-scale plot of v_1 of the jet out to $500 r_j$. Visually $r = 145 r_j$ discerns a point on the image where a constant opening angle is easily measured. Despite the appearance of Figure 7a, however,

a) Jet half-opening angle determination at $r = 145.4 r_j$ for test jet.



b) The establishment of θ_o over time.

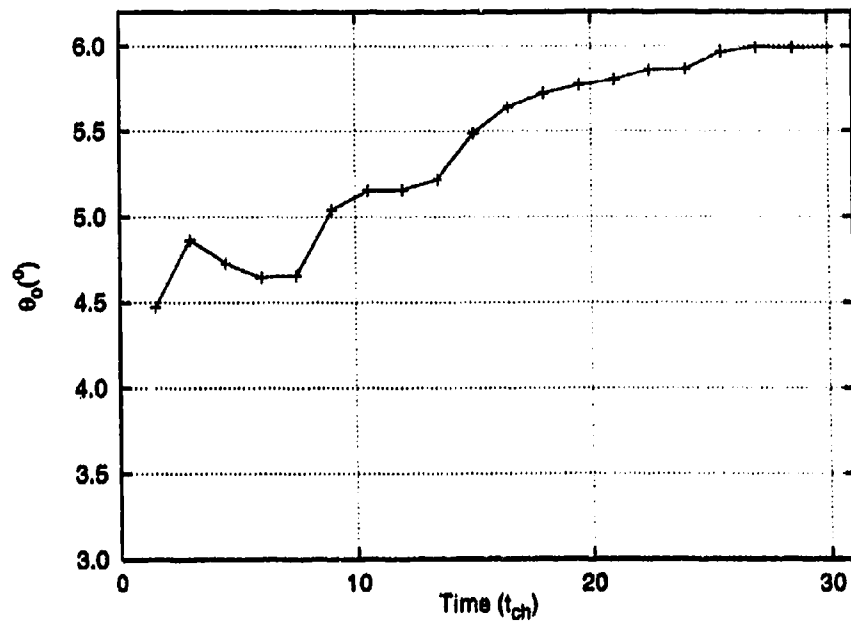


Figure 6: Determination of the half-opening angle of a jet.

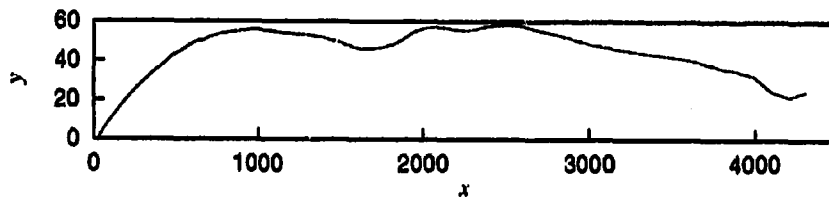
it is impossible to assign a unique opening angle representative of the jet over its entire recollimated length. Figure 7b depicts the edge of the jet (as defined by where the outflow velocity falls by half) along its entire length at $t = 19.5$ (the y -axis has been expanded with respect to the x -axis to view the width of the jet better). Note that the data in Figures 7b and 7c have been presented on a Cartesian grid, with the x -axis coincident with the rotation axis. Clearly the opening angle is not constant along the length of the jet. If the plot is viewed on a log-log scale (Figure 7c), certain features are evident. There is a region of smooth expansion which is not necessarily given by $y \propto x$ (i.e. not a constant opening angle). The jet is eventually affected by the surrounding medium and recollimates, disrupting the smooth expansion. For the purposes of this work, the recollimation point (r_c) is defined as the point where a line indicating constant jet radius from the recollimated region (aside from a few fluctuations) intersects the line representative of the region of smooth expansion. In the simulations presented in the next chapter, it will be found that this smooth region is governed by a power law in x and y . This power law will be fitted to the data in order to determine the recollimation point (see §3.1.3 and Figure 15).

Related to the recollimation point, but not necessarily occurring at the same distance from the core, is a feature prominent in Figure 8a. The solid line depicts the density variations in the jet, ρ_j , along with pressure, p_j (long dash), and temperature, T_j (short dash) plotted against distance along the jet axis. The plot reveals a sharp density minimum, ρ_{min} , at $r_{min} \sim 1600 r_j$. In a region of smooth expansion, ρ_j is well behaved decreasing approximately as the inverse square of the distance from the core. Upon recollimation, the

a) Radial velocity grey-scale image of the first inner 500 r_j of the jet
(darker shades of grey indicate higher velocities).



b) jet edge, linear plot.



c) jet edge, log-log plot.

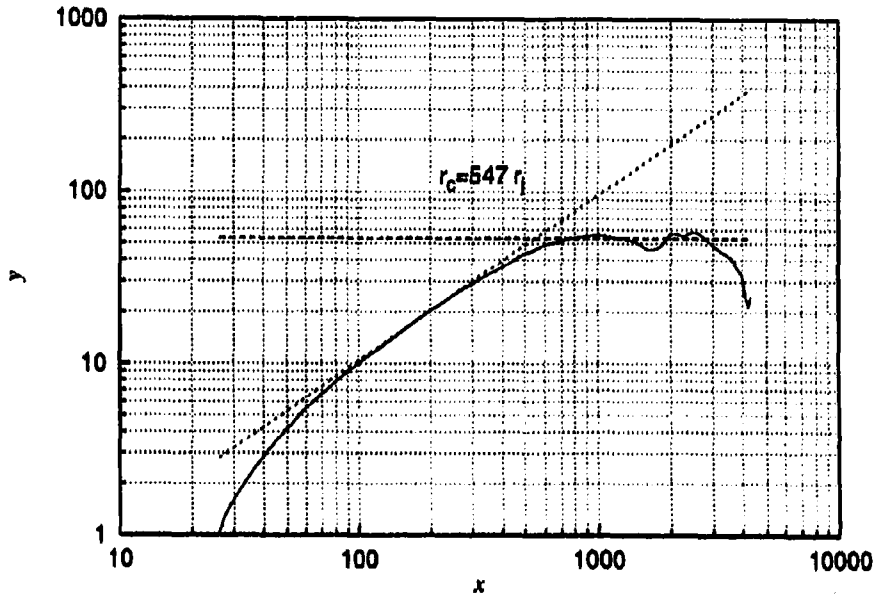


Figure 7: Determination of the recollimation point of a jet.

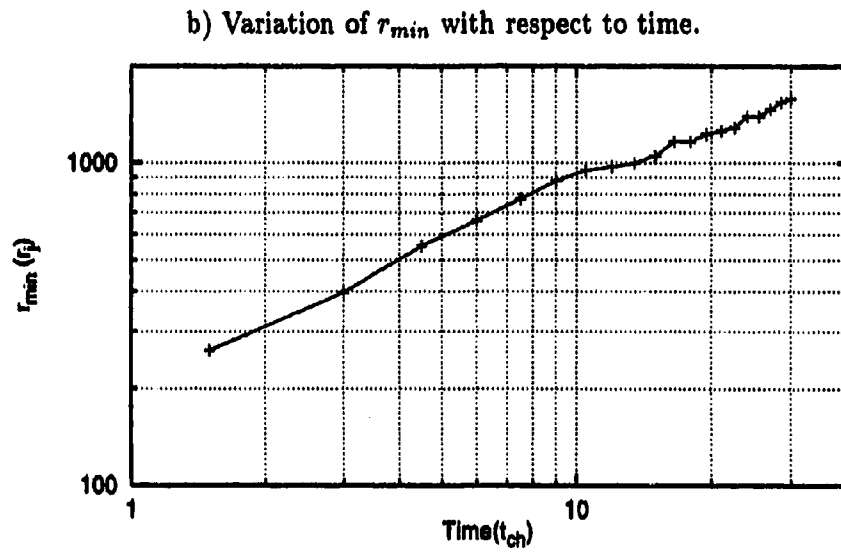
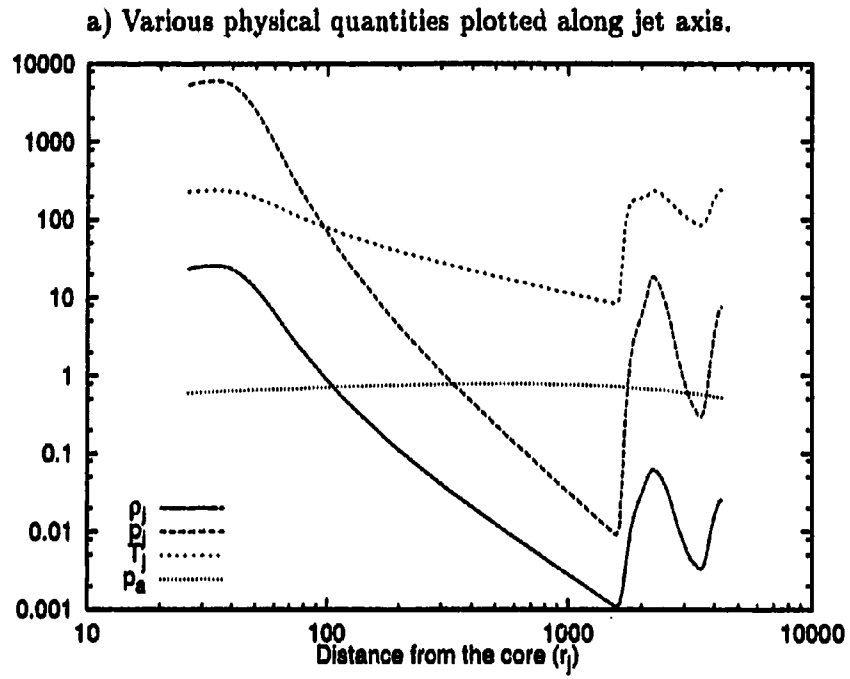


Figure 8: Determination of stability of r_{min} with respect to time, which is an indication of the stability of ρ_{min} .

jet is no longer expanding and a dramatic increase in density is observed as the jet is shocked by the recollimation signal reaching the axis of the jet. It takes time for this signal to reach the axis, and thus r_{min} is usually downstream of the recollimation point (r_c) determined in Figure 7c. Compression of the jet is therefore a dramatic and necessary consequence of recollimation, though does not by itself locate r_c .

Figure 8b plots r_{min} against time (of evolution of the jet), and indicates that even at $t = 30$, r_{min} (and therefore r_c which is less than r_{min}) has yet to reach a steady state (see Figure 17, however, for an example that may have reached a steady state).

From these results, it is obvious the analytically determined initial jet parameters in Table 3 fail to reproduce the observed behavior of the M87 jet. Figure 6 clearly shows a steady-state value of $\theta_o = 6^\circ 00$, and at all points on the curve, $\theta_o > 2^\circ 23$ (the desired value for the M87 jet). In addition, the recollimation point has not yet reached a steady state at $t = 30$, and although not shown, is already well past the position of knot A (at $691 r_j$).

There are numerous factors contributing to the failure of this model. First, the bulk velocity of the jet is very high, so the large momentum of the jet with respect to the ambient medium means there is a large ram pressure, p_r , associated with the jet which has not been incorporated in the analytical calculations. The ram pressure actually dominates the thermal pressure of the jet, resulting in a gross overestimate of the thermal pressure needed to balance the jet at knot A. This is demonstrated by Figure 8a, in which the initial ambient pressure is superimposed over the jet pressure at $t = 30$ (dotted line). After reaching thermal pressure equilibrium with the atmosphere (at $r \sim 350 r_j$), the jet continues

to expand to r_{min} instead of recollimating as the analytical model posits.

Second, at knot A, the jet does not directly interact with the atmosphere but with the cocoon, comprised primarily of hot, shocked jet material. Therefore to predict the correct initial conditions for the jet, the cocoon needs to be computed self-consistently, indicating that numerical experimentation is required.

A third problem exists in the thermodynamics of the computation. It is assumed that a constant value of θ_o exists between the core and knot A. Implicit in this assumption is that the sound speed and/or the bulk flow velocity does not change as the jet expands. A constant sound speed implies constant temperature along the length of the jet (at least until the recollimation point), i.e. the jet must expand isothermally, inconsistent with the jet expanding adiabatically.

This leads to another observation. The jet is expanding *faster* than the *maximum* sound speed of the jet (theoretically at the source of the jet). As the jet expands, it is also cooling, the temperature decreasing as a function of distance from the core (Figure 8a). Since $c_j \propto T_r^{1/2}$ one might have expected the jet to expand *less* than predicted with equation (9). However, as it turns out, the ram pressure (at least the component perpendicular to the jet axis) provides sufficient momentum to the jet transverse to the jet axis to explain the supersonic expansion. Thus, the jet expands faster than that predicted solely from the thermal pressure of the jet.

The failure of the analytical jet model highlights the complex nature of such jet simulations. There are many factors to be considered, the direct consequences of each not

necessarily known and/or calculable in an obvious analytical manner. In such a situation, numerical experimentation is necessary. Therefore, the next chapter presents numerical simulations whose purpose is to identify the region of parameter space in which the initial conditions of the M87 jet lie. From these simulations empirical relationships between physical conditions (density and pressure) and the observables (opening angle and recollimation point) are determined.

3 The search for the M87 jet parameters.

Empirical laws are sought describing the dependence of θ_o and r_c upon initial jet density and pressure at the orifice. The conditions which would best reproduce the M87 observations are interpolated/extrapolated from these relationships and used in a higher resolution simulation to test the validity of the chosen parameters and to investigate the morphology of the jet in greater detail.

3.1 Method of Search

3.1.1 Selection of jet parameters

Thirty jet simulations with different values for the initial pressure and density (Figure 9) were initialized using the methods described in § 2.3.2. Each simulation was evolved to $t = 30$ and assumed an inflow velocity $v = 0.3c$. For each simulation, θ_o and r_c were determined using the techniques described in § 2.2.3 (see extra comments in § 3.1.3 regarding r_c).

The results of the first few jet calculations (out of the 30) aided selection of the initial conditions for follow-up simulations as trends in θ_o and r_c were observed and as the region of parameter space appropriate for the M87 jet became better defined. Table 4 lists the initial conditions and the key results of each simulation.

The general morphology of the majority of the jets is evident in Figure 10, a grey-scale image of the pressure distribution of Jet 10 at $t = 30$ ($\rho = 1.32$, $p = 50.9$; darker shades of grey indicate higher pressures). The white line along the axis of the jet indicates

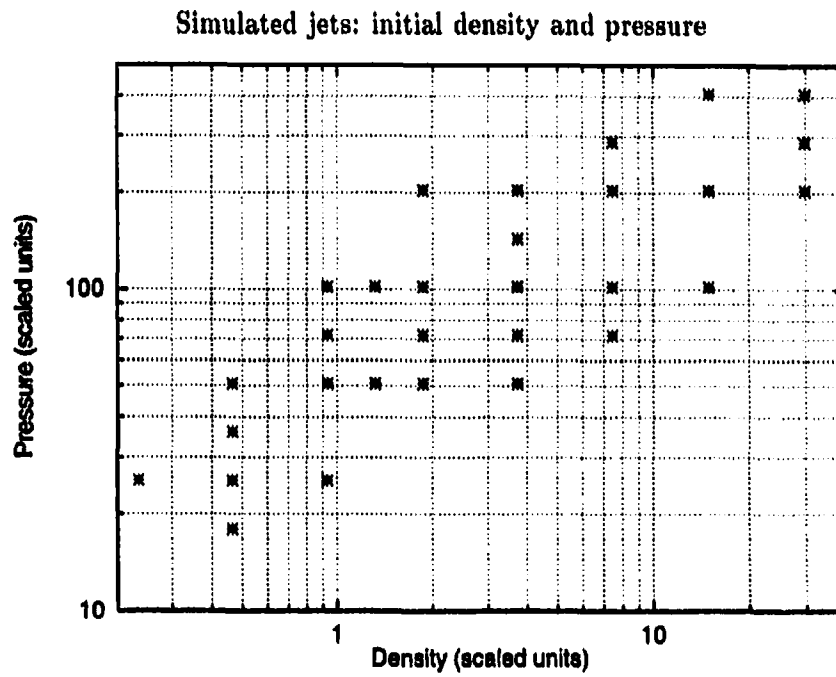


Figure 9: Initial conditions of simulated jets in p - ρ space. Note the quasi-regular spacing on the logarithmic scale.

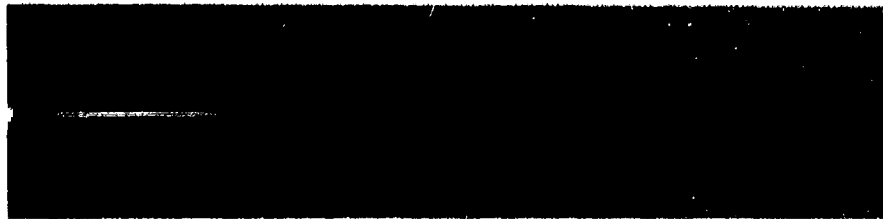


Figure 10: Grey-scale pressure image of Jet 10. Darker shades of grey indicate higher pressures.

Table 4: Initial parameters of the jets, and the key results of the simulations. "†" indicates r_c has yet to reach steady-state, "*" indicates the jet may have run off the grid sufficiently to affect r_c . The parameters ρ_j and p_j indicate initial values at the jet orifice. The measured half-opening angle is θ_o , and the recollimation point is r_c . The average width of the jet after r_c is given by w , while β is the power law index governing the region of smooth jet expansion (see § 3.1.3).

Jet #	ρ_j	p_j	θ_o	$r_c (r_j)$	$w (r_j)$	β
1	0.233	25.4	2.64	166	7.67	0.875
2	0.466	18.0	2.03	372	10.3	0.737
3	0.466	25.4	2.28	353	11.6	0.781
4	0.466	36.0	2.61	340	13.3	0.831
5†	0.466	50.9	3.05	308	14.9	0.890
6	0.932	25.4	2.03	540	13.3	0.721
7	0.932	50.9	2.57	459	15.9	0.789
8	0.932	71.9	2.88	425	17.9	0.835
9	0.932	102	3.30	386	20.2	0.907
10†	1.32	50.9	2.39	464	15.9	0.780
11	1.32	102	3.02	476	20.7	0.844
12†	1.86	50.9	2.25	681	18.0	0.746
13	1.86	71.9	2.48	650	19.7	0.757
14	1.86	102	2.79	572	21.7	0.815
15	1.86	203	3.56	475	26.5	0.907
16	3.73	50.9	2.07	1030	21.1	0.702
17†	3.73	71.9	2.26	968	22.8	0.730
18†	3.73	102	2.48	875	24.4	0.753
19	3.73	144	2.73	790	26.4	0.791
20	3.73	203	3.00	717	29.0	0.840
21	7.46	71.9	2.18	1430	27.1	0.700
22	7.46	102	2.29	1270	28.1	0.728
23	7.46	203	2.70	1140	32.8	0.752
24	7.46	288	2.91	1010	35.1	0.802
25†*	14.9	102	2.23	1880	33.6	0.691
26†*	14.9	203	2.50	1640	37.1	0.725
27†*	14.9	407	2.85	1430	42.7	0.757
28†*	29.8	203	2.40	2260	42.5	0.698
29†*	29.8	288	2.49	2140	45.2	0.726
30†*	29.8	407	2.67	2110	48.5	0.726

where expansion has lowered the pressure considerably. Recollimation occurs where the white section ends (discussed further in §3.2.4). Along the jet, slight variations in pressure indicate the jet is in the process of attaining pressure equilibrium with the cocoon. The area containing the cocoon and shocked ambient is outlined by the dark compressed regions surrounding the jet. Note the long extended nature of the cocoon and the small working surface of the leading edge of the jet. The pressure is the highest in this region.

Note some simulations did not reach steady-state recollimation by $t = 30$ and are indicated by an "†" in Table 4 (e.g. Jets 17 & 18). In some simulations the leading edge of the jet reached the outer boundary. Simulations in which this might have had a significant effect on r_c (and may therefore be suspect) are marked by a "*" in Table 4. A jet reaching the outer edge of the grid is unlikely to affect the determination of θ_o as a signal (i.e. sound wave) from this event would have insufficient time to reach $r = 145.4 r_j$ (where θ_o is measured).

3.1.2 Analysis of trends: opening angle

Figure 11a shows contours of initial jet density (isochores) on a plot of θ_o against initial jet pressure (each point represents a different jet calculation). Hereafter, unless otherwise stated, pressures and densities refer to initial parameters of the jet at the orifice. Each contour shows θ_o increasing as pressure is increased. Qualitatively from equation (4), an increase in jet pressure means a higher sound speed (c_j) and thus a faster expanding jet.

In Figure 11b, constant pressure contours (isobars) are plotted on a graph which shows θ_o decreasing as density increases. From equation (4), $c_j \propto \rho^{-1/2}$, and therefore an increase

Figure 11a: Density contours (isochores) of θ_o vs pressure.

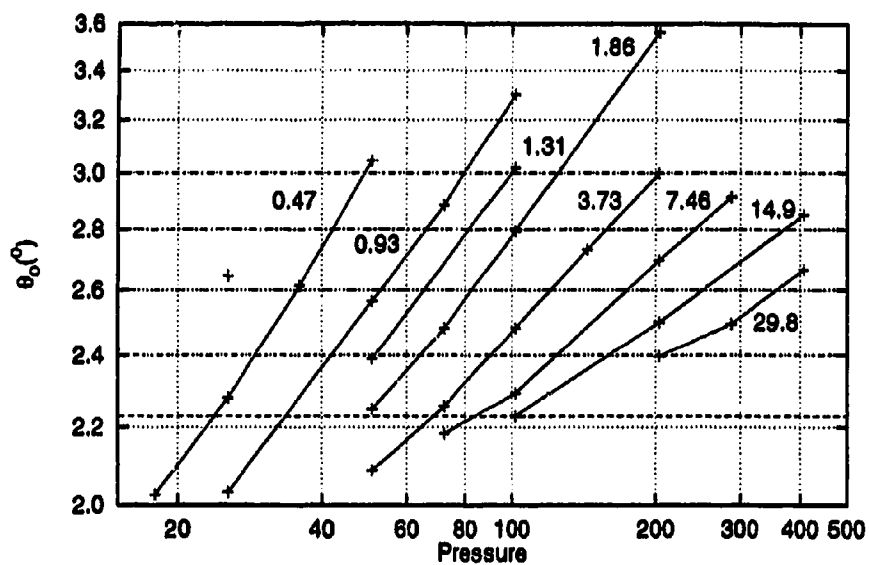


Figure 11b: Pressure contours (isobars) of θ_o vs density.

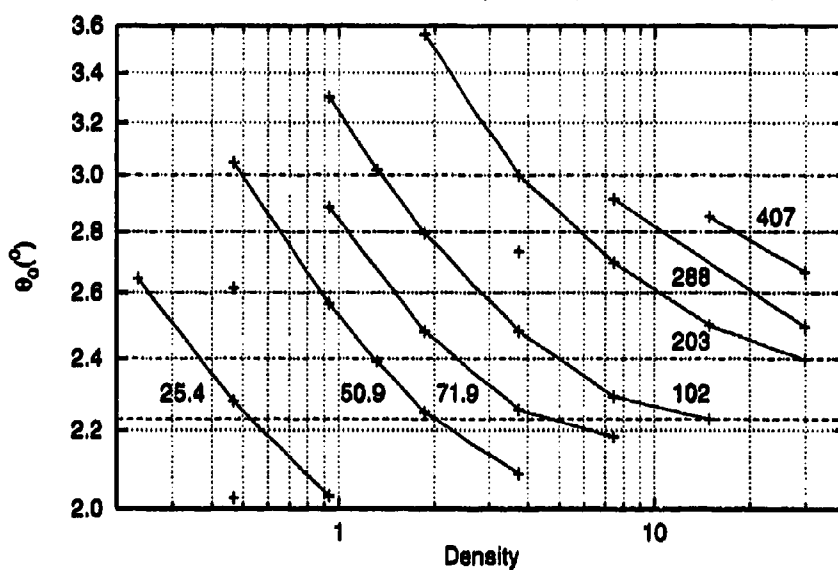


Figure 11: Contours of density and pressure, and interpolation to various θ_o . The contour values are labelled on the plots.

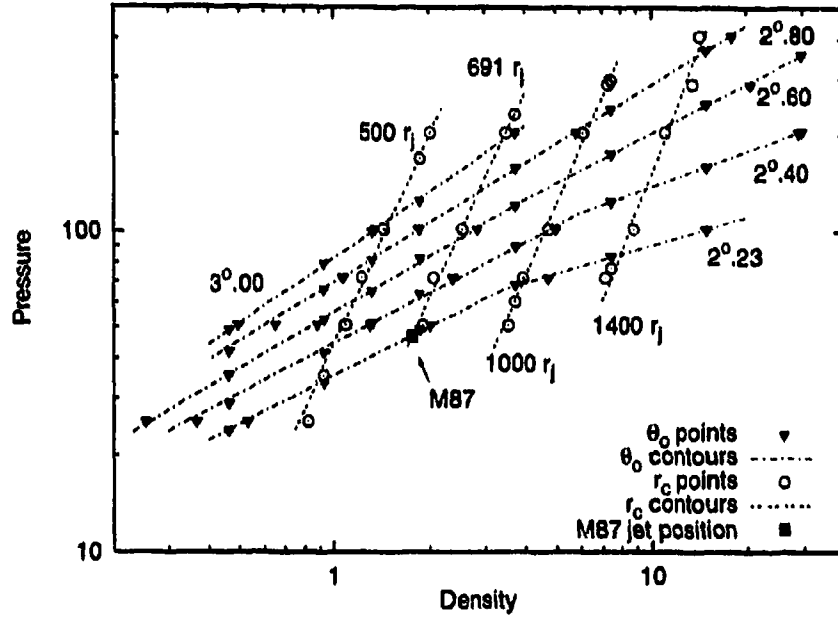


Figure 12: Contours of r_c and θ_o plotted in ρ - p space. The straight lines indicate that power laws govern the relationships.

in density lowers c_j and thus θ_o .

Contours of constant $\theta_o = 2^{\circ}23$, $2^{\circ}40$, $2^{\circ}60$, $2^{\circ}80$, and $3^{\circ}00$ on a pressure-density diagram (Figure 12) were created by interpolating/extrapolating along the density and pressure contours of Figure 11 (note the θ_o values are indicated on the plot). Also plotted in Figure 12 are contours of constant r_c , to be discussed in the next subsection. The $\theta_o = 3^{\circ}00$ and $2^{\circ}80$ contours are represented by straight lines on Figure 12 indicating power laws ($p \propto \rho^\alpha$) with indices of $\alpha = 0.68$ and 0.62 respectively. The $2^{\circ}40$, and $2^{\circ}60$ contours are less well defined. Both define straight lines (power laws) at low densities, but deviate from these power laws at higher densities. For example, the $2^{\circ}40$ contour curves continually downward above $\rho \sim 2.0$.

The last contour, $\theta_o = 2^\circ 23'$, represents the half-opening angle of the M87 jet, and seems to be governed by two distinct power laws, $\alpha = 0.51$ at lower densities and $\alpha = 0.29$ at higher densities with a break between the two at $\rho \sim 3.5$. The origin of these power laws is unclear at present. Nevertheless, the correct parameters describing the M87 jet lie somewhere along the $\theta_o = 2^\circ 23'$ contour, the exact point to be located once relationships describing the recollimation point (r_c) have been determined.

Note that if equation (9) were valid qualitatively, contours of θ_o in Figure 12 should all be described by a power law with index $\alpha = 1$. The failure of equation (9) is further demonstrated by Figure 13, in which $\tan(\theta_o)$ is plotted against c_j/v_j , each point representing a different jet simulation. If the opening angle were in fact the Mach angle, all points should lie on the $\tan \theta = c_j/v_j$ curve in Figure 13 (short-dash line). Clearly this is not the case. However there is a general trend for $\tan \theta_o$ to increase as c_j/v_j increases (on any one density or pressure contour) indicating that the θ_o behaviour is linked to c_j , but not necessarily in the straight-forward manner implied by equation (9).

Evidently, the actual opening angle, θ_o , is always greater than the Mach angle of the jet. Ram pressure may contribute to this phenomena (§ 2.3.3). Figure 14 is a plot at $r_c = 468 r_j$ for Jet 10 showing the thermal pressure (p_{th}) ram pressure (p_\perp) from the component of the velocity perpendicular to the jet axis, and total pressure (P_{tot}) as well as density (ρ) profiles as a function of azimuthal angle. Three distinct regions are evident: jet, cocoon, and atmosphere. Note that p_\perp near the edge of the jet is the main component contributing to the total pressure of the jet. Given the total pressure of the cocoon, p_\perp is

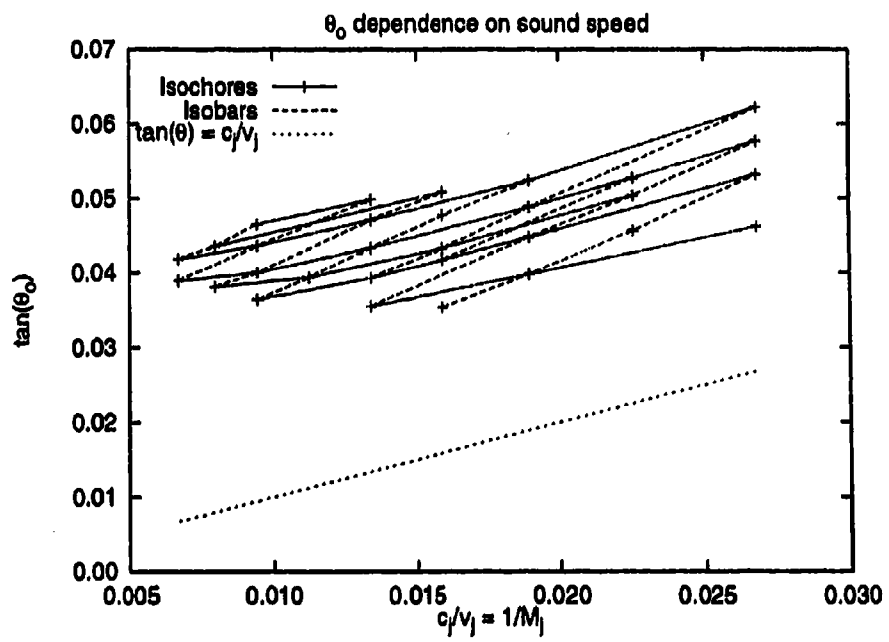


Figure 13: Demonstration of the failure of the Mach angle equation.

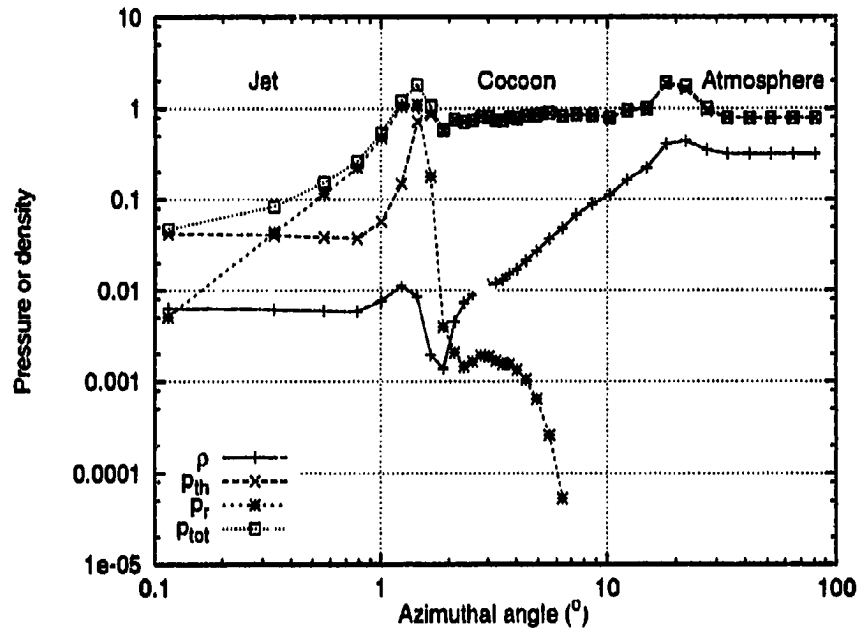


Figure 14: Density (ρ), thermal pressure (p_{th}), ram pressure (p_{\perp}), and total pressure (p_{tot}) as a function of azimuthal angle for Jet 10. The 1D slice is taken at $r_c = 468 r_j$ (See § 3.1.3 and Figure 15). Note the three distinct regions: jet, cocoon, and undisturbed atmosphere.

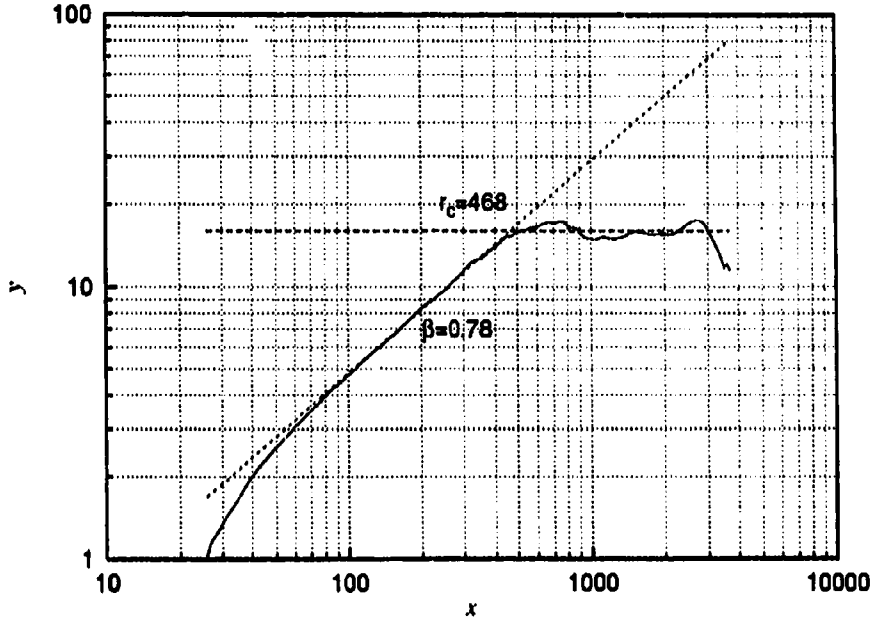


Figure 15: The edge of the jet: determination of r_c of Jet 10 at $t = 30$.

therefore the most important component of pressure which prevents jet collapse prior to r_c .

3.1.3 Analysis of trends: Recollimation point

A slight difference between the morphology of the simulations described in this chapter and the jet simulations discussed in § 2.3 should be noted. Although the latter underwent a period of well-behaved expansion, nowhere was the expansion adequately described by a power law (Figure 7), making it difficult to identify a recollimation point. In contrast, Figure 15 shows a log-log plot of the edge of Jet 10. This jet is typical of those simulated in the parameter search. The straight-line region between $x \sim 100$ and $x \sim 400$ in Figure 15 indicates the expansion can be effectively described by a power law. This section was

fitted by a curve of type $y \propto x^\beta$ with $\beta = 0.78$. The recollimated region was fitted by a constant value of $w = 16 r_j$ (essentially the average width of the jet after recollimation). The intersection of the two curves determine the measured value of r_c ($\sim 468 r_j$ for this jet). Table 4 lists r_c , β and w for each jet.

Note that a *constant* expansion rate for a jet is given by $y \propto x$ (i.e. $\beta = 1$). None of the jets of Table 4 show such a characteristic, further highlighting the failure of the analytical jet model of the previous chapter.

The accuracy of the determination of r_c should be briefly considered. Uncertainties in determining r_c come mainly from one source: choice of limits in fitting w and the power law to the sections of the curves of Figure 15. Variation of the limits of the fit to w and the power law were made to Jet 10, and the resultant changes in recollimation point were compiled. A minimum value of $r_c = 434 r_j$ and a maximum value of $r_c = 495 r_j$ were found, compared to the above value of $r_c = 468 r_j$. Although significant in magnitude, when viewed on the log-log scale of Figure 15, short-term (temporary) fluctuations in the shape of the jet have been found to affect the determination of r_c at least as much. It is therefore difficult to assign a formal uncertainty to r_c other than to keep the above limitations of the process in mind. By simulating a large number of jets, however, any statistical uncertainties are minimized by allowing r_c contours to be fit to as many data points as possible (Figure 12). A similar statement can be made for the determination of θ_o . Physical fluctuations in the azimuthal size of the jet will be the main contributor to any uncertainties in the determination of θ_o , not in the interpolated determination of θ_o .

(Figure 6a), which is quite accurate. By fitting contours to as many data points as possible, statistical uncertainties induced by these physical fluctuations should be reduced.

Figure 16 shows isochores on a plot of r_c against pressure and isobars on a plot of r_c against density. From these data one can see that r_c decreases gradually with increasing pressure (at constant density) and r_c increases sharply with increasing density (at constant pressure). Denser jets provide greater ram pressure which, as discussed in §2.3, helps the jet to resist recollimation. Further, a higher density reduces the internal sound speed of the jet, decreasing θ_o and focusing outflow, resulting in a further increase in ram pressure. Therefore the jet must travel further and undergo more expansion (to decrease the density and ram pressure) before external material can recollimate the jet. In contrast, increasing pressure at constant density elevates c_s , increases θ_o , and thus decreases ram pressure. The jet is less focused allowing the jet to recollimate sooner.

Figure 16 must be viewed with some caution because for some simulations (labelled with a “†” in Table 4), the recollimation point has yet to reach steady-state. However the results still give an adequate qualitative outline of the situation. With this caveat in mind, interpolations to $r_c = 500, 691$ (knot A), 1000, and 1400 r_j were performed on the density and pressure contours of Figure 16 (the r_c values are indicated in the plots), and the results plotted in Figure 12 (along with the θ_o interpolations). The relationship between pressure and density along contours of r_c are evidently given by a power law as indicated by the straight lines on the logarithmic plots. Table 5 lists the power law index, δ , derived for each r_c contour.

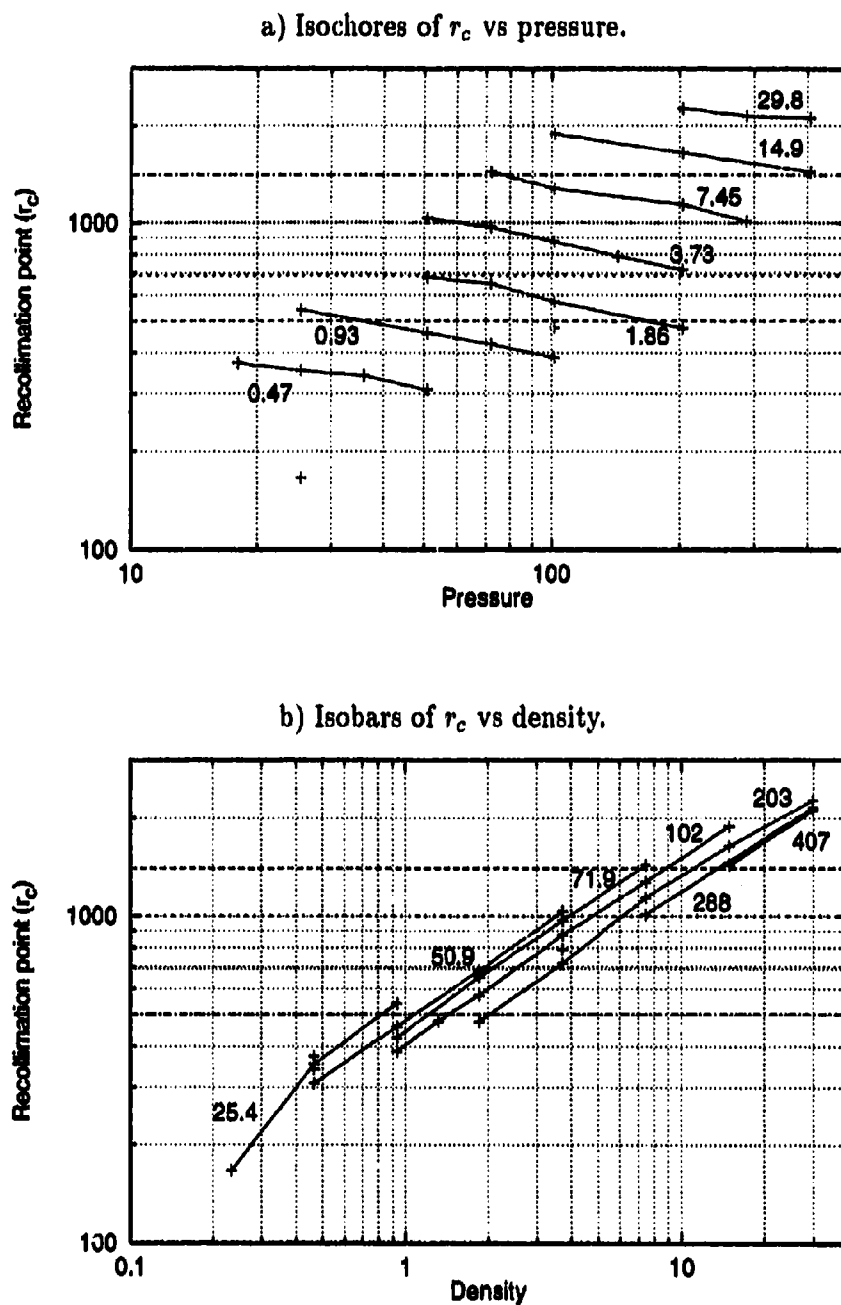


Figure 16: Contours of density and pressure, and interpolation to $r_c = 500, 691$ (knot A), 1000, and 1400 r_j . The contours values are labelled on the plots.

Table 5: Listing of power law indices, δ , found for the r_c contours of Figure 12.

$r_c(r_j)$ contour	index δ
500	2.15
691	2.13
1000	2.30
1400	2.55

Built into the analytical model of the previous chapter is the assumption that the recollimation point is determined solely by the initial jet pressure and, in particular, is independent of initial jet density. Thus, for a fixed pressure, equation (10) implies the jet angle θ_o will be different for different initial densities, i.e. $\rho \tan^2 \theta_o$ remains a constant. If this argument held, contours of constant r_c in Figure 12 would be horizontal lines following the isobars, and all isochores of Figure 16a would be overlaid on a single curve. In fact, density affects r_c considerably more than pressure, highlighting the failure of the analytical model and that ram pressure plays the most important role in determining r_c .

3.1.4 Final identification of parameters describing M87

It is now possible to identify the initial parameters for the M87 jet. In Figure 12, the $r_c = 691 r_j$ and $\theta_o = 2^\circ 23'$ contours cross at $\rho = 1.76$, $p = 46.9$. A jet simulated with these initial conditions should reproduce the observed values of r_c and θ_o (in 2D) for M87 to a reasonable degree of accuracy. To confirm this hypothesis, such a simulation was performed, initialized as the other jets in Table 4 were, except that the jet was evolved until $t = 45$ in order to test the stability of the recollimation point and opening angle. Figure 17 plots θ_o

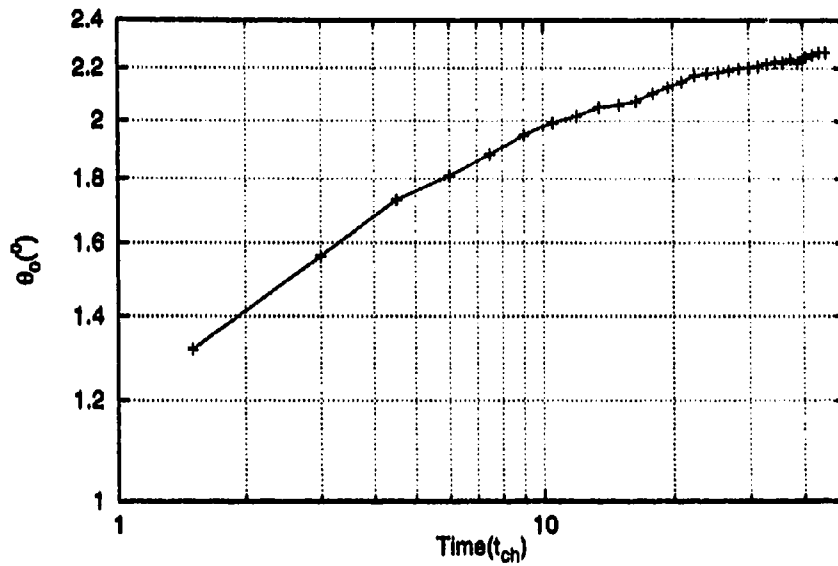
and r_{min} (which tests the stability of r_c) as functions of time. It is questionable whether steady-state has been reached. The jet has evolved slightly beyond the $t = 30$ values of $r_c = 686 r_j$ and $\theta_o = 2^\circ 20'$. The $t = 45$ values are $r_c = 746 r_j$ and $\theta_o = 2^\circ 27'$.

A comparison of Figure 17b with similar plots for the other jet simulations presented in this chapter suggest that r_c has reached steady-state (at around $t = 35$), although this cannot be stated conclusively without evolving the system further. It is more doubtful that θ_o has reached steady-state. However, even if θ_o continues to grow, the trend at $t = 45$ suggests it will do so at a diminishing rate given the logarithmic scale of the plot.

Note that $t = 45$ corresponds to $\sim 4.3 \times 10^5$ yr compared to an age for the M87 jet of $\sim 10^6$ yr (a lower-limit estimated by Bicknell & Begelman, 1996). As such, all of the jets in this survey are young compared to the M87 jet. The establishment of steady-state (or near steady-state) by $t = 30$ for most of the jets suggests that the inner jet of M87 has either reached a steady-state or is evolving extremely slowly at the present time. This is the prime motivation behind finding the initial parameters of a jet which eventually reproduce steady-state values of θ_o and r_c .

Table 6 summarizes the results for this jet, both at $t = 30$ for comparison with Table 4, and at $t = 45$. The closeness of the $t = 30$ values to the predicted values of $r_c = 691 r_j$ and $\theta_o = 2^\circ 23'$ demonstrates the usefulness and precision with which predictions can be made using this method. However, so far all calculations have been performed on low-resolution (LR) grids. For the structure of the jet and cocoon to be more thoroughly investigated (e.g. internal shocking of the jet, evolution of a hot spot, etc.) a high-resolution (HR)

a) Evolution of θ_o for the candidate jet.



b) The possible establishment of a steady state value of r_{min} for the candidate jet, indicating r_c has also stabilized.

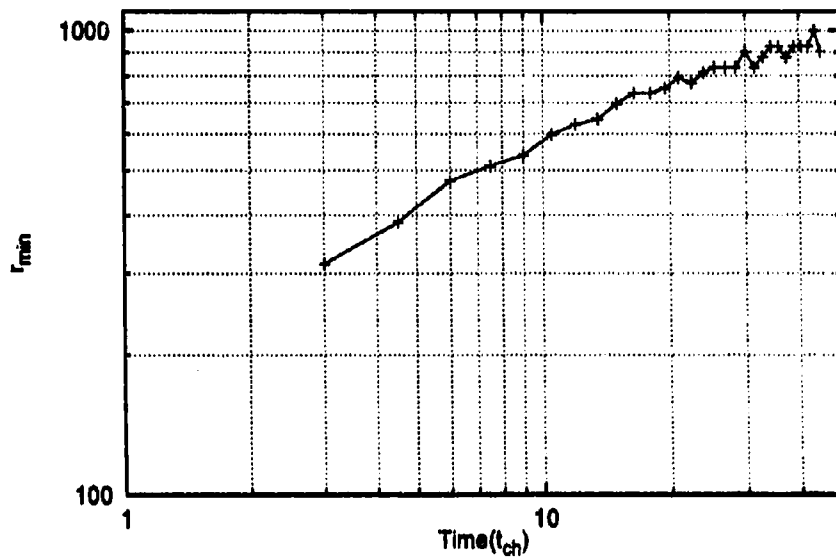


Figure 17: The determination of the steady-state results for the candidate jet.

Table 6: The initial conditions and results for the M87 candidate jet (low-resolution) simulation.

t (t_{ch})	ρ_j	p_j	θ_o	r_c (r_j)	w (r_j)	β
30	1.76	46.9	2.20	686	17.8	0.747
45			2.27	746	19.8	0.755

simulation must be performed utilizing the initial conditions of the candidate jet from Table 6.

3.2 The M87 jet: high-resolution simulation

3.2.1 Initialization

To explore the morphology of the jet at higher resolution, a 400×120 zone polar grid was initialized (Figure 18). The radial direction was resolved by 400 geometrically expanding zones from the inner boundary outward. The grid ran from 50 pc ($25.7 r_j$) to 8500 pc ($4367 r_j$), identical to the low resolution grid but with grid resolution from $0.30 r_j$ to $55.7 r_j$ respectively. The angular direction was resolved by 120 zones, 45 zones resolving the first 1.5 angular jet radii ($3^\circ 35'$, $0^\circ 074/\text{zone}$) and 45 geometrically expanding zones resolving the region from $3^\circ 35'$ to 60° (grid resolution $0^\circ 074/\text{zone}$ to $5^\circ 3'/\text{zone}$). Thirty zones resolved the region from 60° to 90° (resolution $1^\circ/\text{zone}$; this region of the grid is not affected significantly by the jet, so the sudden increase in grid resolution should not affect the results appreciably). Thirty zones resolved the jet radius at the inner boundary.

Note that this is essentially double and triple the resolution in the radial and azimuthal

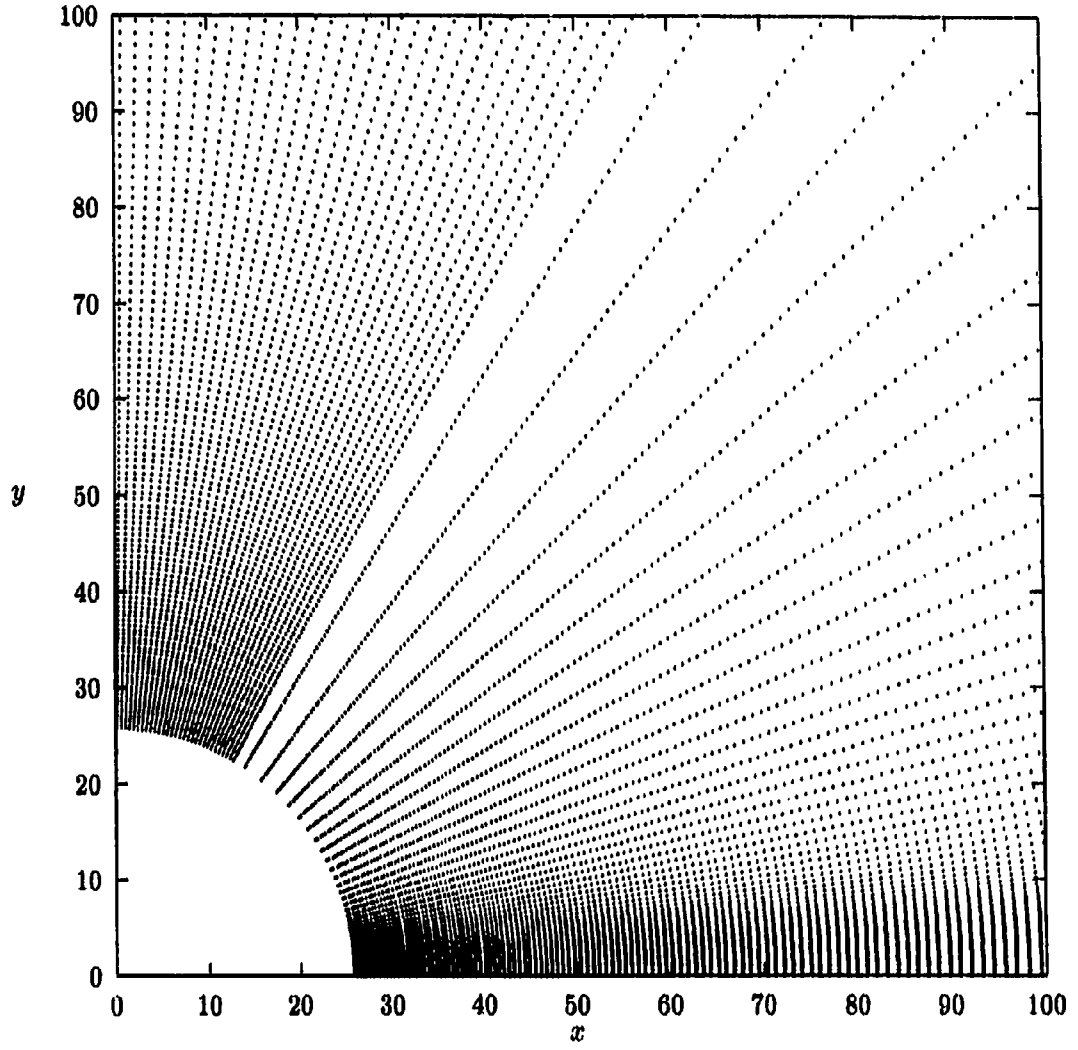


Figure 18: The inner $100 r_j$ of the grid used in in the HR simulation, the points marking the centre of each zone. The jet is launched parallel to the x-axis. Distances are in units of r_j . Note that the actual grid extended to $4367 r_j$ (8500 pc).

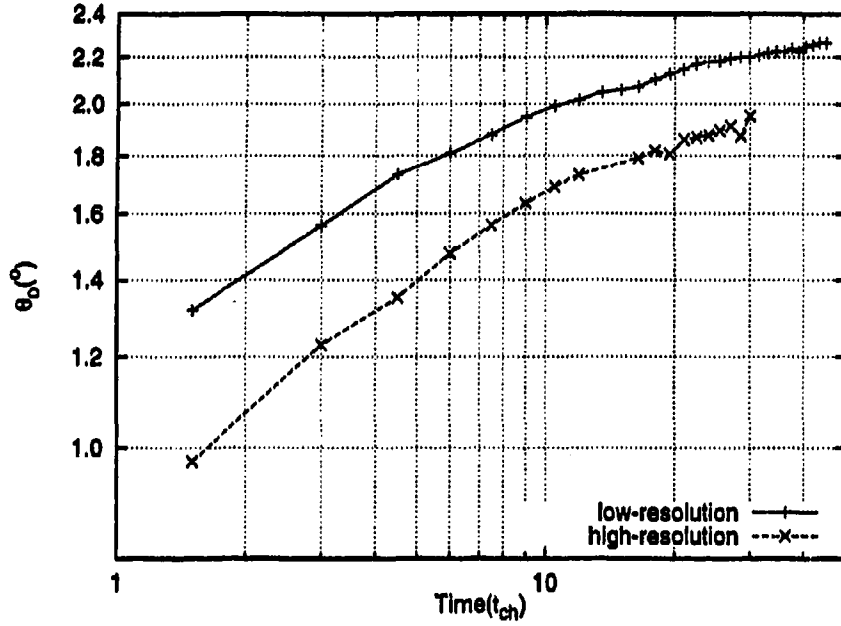


Figure 19: Comparison of HR and LR simulations: evolution of θ_0 with respect to time.

directions respectively over the LR simulations. The jet was evolved to $t = 30$ (taking ~ 128 hours on a Sparcserver 20 Model 612 MP computer).

3.2.2 Results: opening angle

Figure 19 shows the evolution of the opening angle with respect to time. It shows both the HR and LR data for easy comparison. It is clear that the opening angle is sensitive to the grid resolution and that the HR jet has a considerably smaller opening-angle at $t = 30$ ($1^{\circ}95$ versus $2^{\circ}20$; the high-resolution jet was not continued to $t = 45$ since the jet reached the outer boundary of the grid considerably earlier than expected). This is an unfortunate effect of the use of low resolution grids to hasten the process of determining the M87 jet

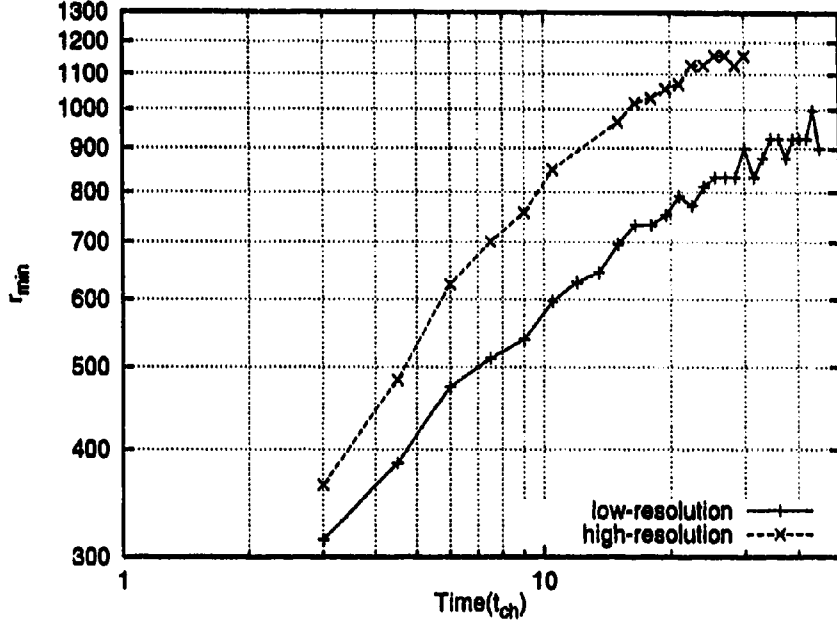


Figure 20: Comparison of HR and LR simulations: evolution of r_{min} with respect to time.

parameters. Note also that θ_o does not appear to have reached steady-state by $t = 30$ in the HR run.

3.2.3 Results: recollimation point

Figure 20 shows an analysis of r_{min} to test the stability of the recollimation point, r_c . Note that r_{min} is considerably larger at all times in the HR simulation than in the LR simulation. This is probably caused by the decreased opening-angle which has focused the jet more, increasing the forward ram pressure of the jet, and allowing it to travel further and faster. It is significant that the leading edge of the jet reaches the outer boundary at $t \sim 15$, only 58% of the time required for the LR to do the same (at $t \sim 26$). Nevertheless, although

not conclusive, the recollimation point may have reached steady-state, as indicated by the stability of r_{min} between $t = 25$ and $t = 30$ in Figure 20. Remarkably, this corresponds to $r_c = 647$ at $t = 30$, indicated in Figure 21, which is actually a *smaller* recollimation distance than for the LR jet ($686 r_j$). The measured width of the jet, $w = 14.7$, indicates a thinner jet, consistent with the smaller opening angle and smaller value of r_c found in the HR calculation. If the recollimation point depends in part on the ram pressure originating from the component of the velocity perpendicular to the flow direction (caused by the jet expansion), then the results are consistent with such a picture. The smaller opening angle means a smaller component of the velocity is directed perpendicular to the main flow of the jet, resulting in a smaller value of r_c as the cocoon is not required to “redirect” as much flow back towards the axis of the jet to achieve recollimation.

The values obtained for r_c and θ_o for the HR simulation do not match the opening angle and recollimation point of M87, and underestimates the required values by 10% and 6% respectively. It, seems certain however, that the correct region of parameter space has been located (over-pressured, slightly underdense) and qualitative interpretations of the results should still be applicable. It has been observed that most jets in this survey have similar enough morphologies (other than different θ_o and r_c values) to make observations of one particular jet applicable to the majority. In other words, the HR jet should still provide valuable qualitative insight into the jet system.

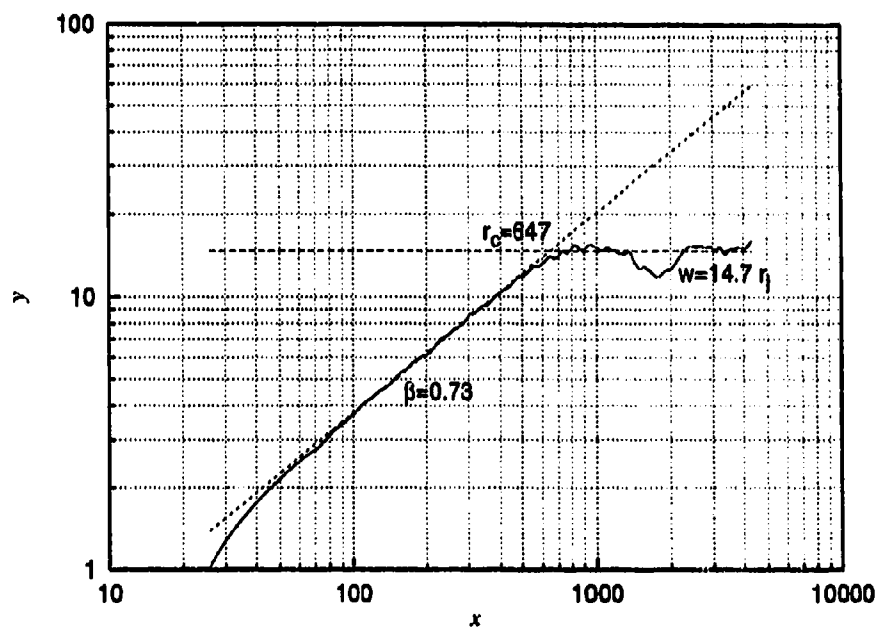


Figure 21: Determination of r_c for HR simulation at $t = 30$.

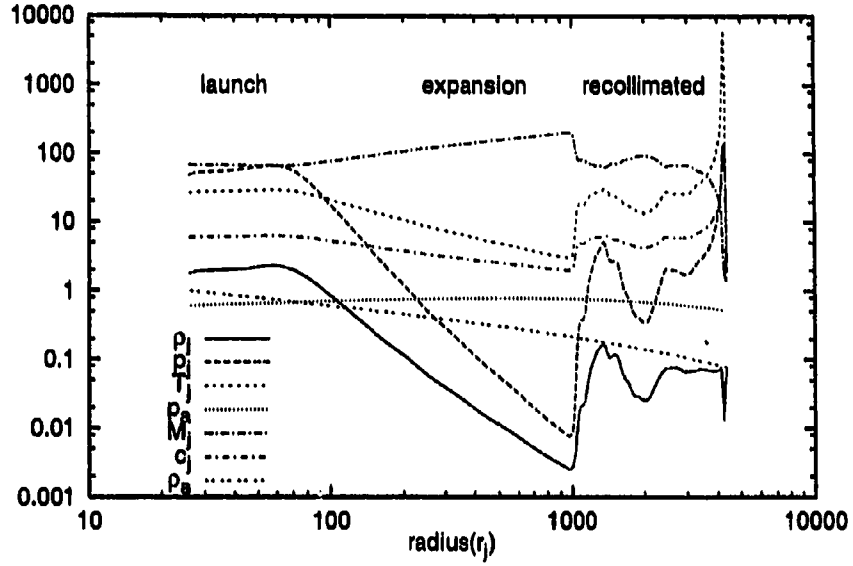
3.2.4 Results: Overall jet morphology

Figure 22 shows a number of physical quantities of the jet plotted as a function of distance from the core at $t = 15$ (when the leading edge of the jet reaches the outer boundary) and $t = 30$ (the end of the simulation). The units of the axis are in the scaled units appropriate for the particular quantity in question. Figure 23 is a plot of velocity along the axis of the HR jet at $t = 30$.

Evidently, there are three separate phases of jet evolution: launch, expansion, and recollimation. During the launch phase, the jet material is establishing the correct expansion rate, as initially the jet is launched parallel to the jet axis. The expansion phase is characterized by the power law index, $\beta = 0.73$, in Figure 21. Recollimation occurs at $r_c = 647 r_j$ at $t = 30$. The recollimation signal (converging sound waves) reach the axis of the jet at $r_{min} = 1160 r_j$, causing abrupt changes in all physical quantities in Figure 22. These features can also be viewed in grey-scale images (Figure 24) of pressure, density and velocity divergence of the jet at $t = 15$ just before the leading edge of the jet leaves the grid, and are therefore directly comparable to the profiles of Figure 22a.

In Figures 22a and 24, $r_{min} = 960 r_j$ and indicates the beginning of the recollimation phase. After r_{min} , the jet pressure experiences alternating periods of overpressure/underpressure with respect to the atmosphere (indirectly through the cocoon) as the jet tries to establish pressure equilibrium with the surroundings. For the most part, the fluctuations are too small to be seen in the grey-scale plots, but they are quite visible in the jet-axis profiles. The initial expansion is quite visible, however, particularly in Fig-

a) $t = 15$ just before the leading edge of the jet reaches the outer boundary.



b) $t = 30$ showing the profiles at a later epoch.

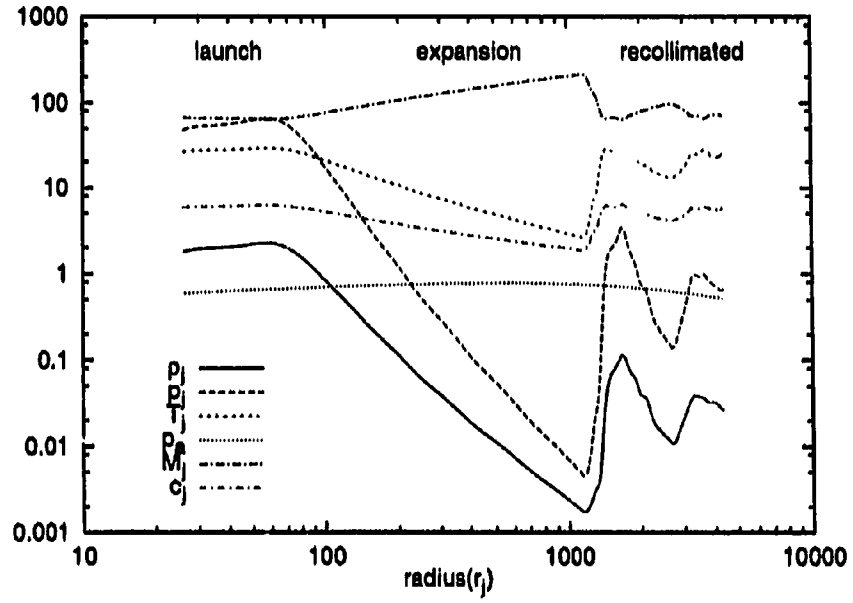


Figure 22: Profiles of various physical quantities along the axis of the jet. The units of the y-axis are in scaled units of the quantities plotted.

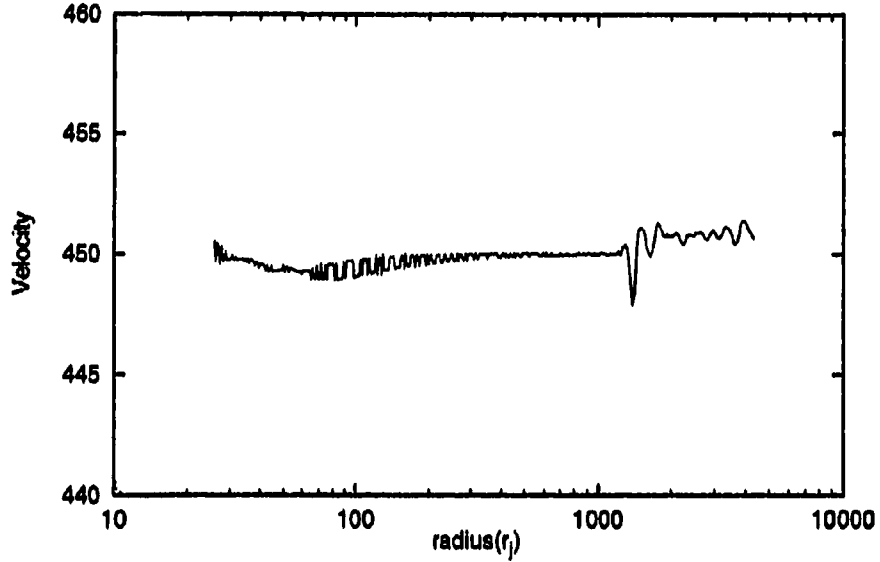


Figure 23: Velocity profile along the HR jet axis at $t = 30$.

ure 24b as the white expanding region along the jet axis indicating a lower pressure than the surrounding cocoon. The initial overpressured region after recollimation and the second underpressured region are also visible. More detail is visible in the grey-scale images of velocity divergence < 0 , which is a good indicator of shock structure (Figures 24e and f). The dark regions along the jet are areas of high negative velocity divergence, and indicate shocks from successive periods of contraction. They are similar in appearance to those observed in the simulations of Norman, Smarr, and Winkler (1985), except the jets presented in this work are at much higher Mach numbers and thus, after the jet is shocked, subsonic flow is not observed. The criss-crossing structure surrounding the jet outlines the cocoon quite clearly from the smooth region of the shocked ambient material, which in turn is separated

a) Pressure, full jet.



b) Pressure, inner 2000 r_j .



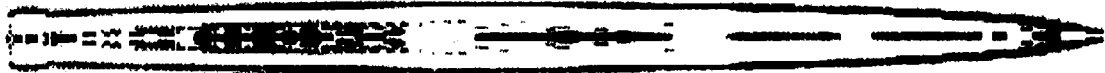
c) Density, full jet.



d) Density, inner 2000 r_j .



e) Velocity divergence < 0 , full jet.



f) Velocity divergence < 0 , inner 2000 r_j .

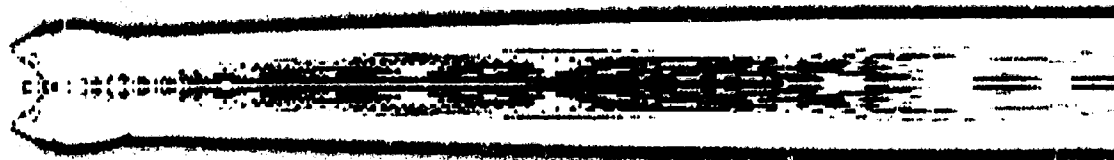


Figure 24: Grey-scale images of the pressure, density and velocity divergence of HR jet at $t = 15$. Darker shades of grey correspond to greater pressures or densities or negative $\text{div}(\mathbf{v})$.

from the undisturbed atmosphere by the narrow bow shock.

The grey-scale plots reveal a jet which is not inhibited greatly by the atmosphere. The long, thin morphology of the cocoon, and the very small working surface between the jet and atmosphere indicate the jet/atmosphere interface is advancing quite rapidly. Given that the jet leaves the grid at $\sim 15 t_{ch}$, this corresponds to an average advance speed for the working surface of $\sim 300 r_j/t_{ch}$ (compared to the jet speed of $450 r_j/t_{ch}$). This helps explain the absence of large diffuse cocoons that might have been expected—there has yet to be any significant “splash back” of material from the working surface and the leading edge of the jet is moving too fast to leave any significant amount of material behind. Thus, the cocoon is long and thin, and does not resemble the M87 radio lobes at all.

It is obvious that the jet is highly stable against disruption. This can be explained by the M_j (long dash-dot) and c_j (short dash-dot) curves of Figure 22. Figure 23 shows that, except for a few minor fluctuations, the velocity of the jet remains constant, and thus M_j will be determined primarily by the jet temperature. As the jet undergoes expansion, the pressure and density decrease. Since the pressure decreases faster than the density, the temperature (short-dash) also decreases (as $T_j \propto p_j/\rho_j$), lowering the internal sound speed and increasing M_j . This helps stabilize the jet against disruption (Hardee 1982). Recollimation heats the jet up, but not to temperatures significantly greater than jet temperatures at the core. Thus the Mach number of the jet remains high and stable against disruption. Left to its own devices, the jet should establish pressure equilibrium with the cocoon. Although not particularly visible in Figure 24 because of the poor resolution of the image, there is

some evidence in the regions of high compression along the axis of the jet of oblique “criss-cross” shocks (Norman, Smarr & Winkler 1985). The poor resolution of the grid in these regions along the jet axis, particularly in the radial direction, makes positive identification and analysis uncertain. They should become more prevalent once the jet actually reaches pressure equilibrium with its surroundings, and may be what finally disrupts the jet (by increasing the jet temperature and reducing M_j sufficiently for the jet to be vulnerable to disruption).

Note that the jet has already advanced well beyond the disruption point for the M87 jet which occurs at about knot C, roughly twice as far from the core as knot A or less than half-way across the length of the grid. It is hypothesized that in order to disrupt the jet, 3D calculations and the extra degree of freedom such calculations would allow are necessary. In 3D, various elements can be added to the simulation which will serve to destabilize the jet. For example a cross-wind might be added to the atmosphere flowing perpendicular to the flow of the jet, which the VLA images of Hines, Owen & Eilek (1989) suggest may exist. Also, 3D jets are more subject to certain destabilizing factors such as higher-order Kelvin-Helmholtz instabilities (which serve to break the jet symmetry), and internal shocks which tend to affect the flow to a greater degree than in 2D.

However, even then, the formidable ram pressure of the jet would be difficult to overcome. In the grey-scale image of density in Figure 24, the jet is only slightly under-dense relative to the undisturbed ambient atmosphere as the jet reaches the edge of the grid (see Figure 24a where the density of the ambient medium is plotted for comparison), which

indicates that ram pressure on the cocoon/atmosphere is still large. The fact that the jet has managed to flow so far without even a hint that it may disrupt is a major problem, and the instabilities that could be introduced in a 3D calculation may or may not be enough to break the jet symmetry and destabilize the flow. If 3D simulations fail to disrupt the jet, then it will be necessary to find other ways to explain the M87 jet.

The mass flux, \dot{m} , along the jet is easily calculated from

$$\dot{m} = \pi r_j^2 v_j \rho_j \quad (13)$$

by using the initial conditions of the jet at 50 pc. In real units, the values are $r_j = 1.95$ pc, $v_j = 0.3c$, and $\rho_j = 8.82 \times 10^{-25} \text{ g cm}^{-3}$, corresponding to $\dot{m} = 0.014 M_\odot \text{ yr}^{-1}$. This is smaller by about two orders of magnitude than the estimated $1 M_\odot \text{ yr}^{-1}$ of matter falling into the SMBH via the cooling flow (Stewart *et al.* 1984).

It is estimated that the non-stellar radio to optical spectrum of the M87 jet and radio lobes have a total synchrotron power output of $8 \times 10^{35} \text{ W}$ (Turland 1975). The jet power $P_j = 3.6 \times 10^{36} \text{ W}$ of the HR jet is easily calculated from

$$P_j = \frac{1}{2} \pi r_j^2 \rho_j v_j^3, \quad (14)$$

which is sufficient to account for the value of P_T . In particular, since there is probably an undiscovered counter-jet delivering a similar amount of energy to the eastern lobe, the efficiency,

$$\epsilon = \frac{P_T}{2P_j}, \quad (15)$$

for converting P_j into synchrotron radiation would be approximately 0.1.

This calculation and the evaluation of \dot{m} are meant primarily to provide an independent check on the value of the jet density determined in previous section. In both cases, the value of ρ_j yields reasonable results.

4 Summary and Conclusions

4.1 Jet morphology

The parameter search of Chapter 3 has successfully identified the region of parameter space in which the initial conditions for the M87 jet must lie (given the present observations). Low resolution (LR) simulations reveal that a jet with $\rho = 1.76 (9 \times 10^{-25} \text{ g cm}^{-3})$, $p = 46.9 (9 \times 10^{-10} \text{ Pa})$ reproduce the opening angle and recollimation point at $t = 30$ with acceptable accuracy. These numbers evolve slightly after $t = 30$, but the results from the rest of the jet simulations suggest that if the jet has not reached steady-state values by $t = 45$, it will do so shortly thereafter or at most increase at a steadily diminishing rate with respect to time. As the jets are young compared to the estimated age of the M87, it is deduced that the inner jet of M87 has either reached a steady-state, or is evolving slowly if at all. Note that this is based on the assumption that the atmosphere is not evolving in such a way that affects the morphology of the inner jet.

High resolution (HR) simulations with the same initial conditions produce a smaller opening angle ($\theta_o = 1.95$), and recollimation point ($r_c = 647$) than the LR calculation, and indication that there remain some resolution effects in the LR survey. However, the trends observed in the parameter search suggest that the true values are contained within those already computed at low resolution, and that qualitative analysis of the HR jet will still provide important insight into the M87 jet (*e.g.* cocoon and jet structure, *etc.*) A HR jet that would reproduce the opening angle and recollimation point of the M87 jet requires a higher density and pressure than the one simulated in the previous chapter.

Rough interpolations/extrapolations predict that initial conditions $\rho \sim 2.5$, $p \sim 82$ might reproduce the correct opening angle and recollimation point at high resolution. Interpolations/extrapolations on the contour map of Figure 12 were made to find the point which corresponded to a LR jet of $\theta_o = 1.95$ and $r_c = 647$. This corresponds to $p \sim 27$, $\rho \sim 1.2$. Pressure and density ratios of 1.7 and 1.4, respectively, therefore exist between HR and LR jets of the same θ_o and r_c values. It is assumed that a $\theta_o = 2.23$, $r_c = 691$ jet is affected by similar ratios on the transition from LR to HR, thus giving the pressure and density values quoted above. However, the numbers are based on assumptions that need to be verified, and are further complicated by the fact that the $p \sim 27$, $\rho \sim 1.2$ region of parameter space in LR has yet to be thoroughly explored. Certainly, however, these values should serve as a starting point for a limited parameter search at HR if r_c and θ_o values of M87 are not immediately reproduced. Experience has shown that by expanding the search gradually by factors of $2^{1/2}$ in p and ρ , the details of a contour map of θ_o and r_c such as Figure 12 should be resolvable, and should also efficiently locate the correct values.

Given that high resolution calculations reveal that there remain some resolution effects in the LR survey, the use of the LR simulations may be questioned. However, resolution effects are more than offset by the much shorter computational time required to evolve a jet to $t = 30$ in LR than in HR. A high resolution calculation takes ~ 5 days while a LR calculation takes ~ 8 to 9 hours. This allows parameter space to be explored much more efficiently in LR, and ultimately allows the parameters of a particular source to be found much more quickly overall.

Jets in the general area of parameter space describing the M87 jet have many things in common: a high Mach number, high velocity jet which is overdense, overpressured and therefore expanding (note that these are more or less as predicted from the discussion of Chapter 1). They are contained in an atmosphere with density and pressure gradients which promote jet stability. All of these factors and the imposed geometry conspire to produce a jet which is ultra-stable, and consequently the disruption of the jet and the large "fluffy" cocoon observed in Virgo A are not reproduced by these simulations. If the simulations were allowed to continue longer (on a large enough computational grid), these features may be reproduced but would appear well beyond the distances observed in M87. Instead the simulation presented in § 3.3 produces a thin, long, hot cocoon surrounding the whole length of the jet. The grey-scale images of Figure 24 reveal the jet going through alternating periods of high and low pressure with respect to the atmosphere, with shocks interspersed in between. There is evidence of "criss-cross" shock structure present in the highly compressed regions along the jet axis, although it cannot be seen in the images of Figure 24 because of low image resolution. The shocks should become more prevalent once pressure balance with the cocoon is achieved, and may serve to eventually disrupt the jet. Disruption would, however, occur at distances further from the core than observed in M87. Three dimensional (3D) calculations, and the extra degree of spatial freedom they entail may allow a mechanism by which the jet can be disrupted at the appropriate distance from the core (*e.g.* Kelvin-Helmholtz instabilities in the jet and/or the use of cross-winds, *etc.*) If this can be achieved, it is hypothesized that the production of the radio lobes may follow.

However there are no guarantees this will happen, and even 3D effects may not be able to overcome the apparent high stability of the jet.

The high computational costs (in time) of performing 3D simulations may also pose a problem requiring that any parameter search be of limited scope. Therefore, if significant differences in θ_o and r_c between 2D and 3D calculations develop as they did between the LR and HR 2D calculations, then it may be difficult to locate the correct region of parameter space required to describe the observations.

4.2 Opening angle

Contours of constant opening angle (θ_o) on a pressure—density diagram (Figure 12) were found to describe power laws $p \propto \rho^\alpha$. Values for θ_o were found in all cases to be larger than the Mach angle [Equation (9) and Figure 13]. A correlation between opening angle and sound speed was shown to exist (as c_j increases, so does θ_o along any particular isochore or isobar), but an analytical description from first principles remains unspecified.

This work has shown that more factors contribute to the opening angle of a jet than originally thought, and that the Mach angle representation is much too simple to describe the opening angle successfully. For example, the ram pressure of the velocity component perpendicular to the jet axis provides sufficient momentum to allow the jet to expand faster than that determined by the Mach angle.

Regions of well-behaved jet expansion were shown to be described well by a power law in x and y , *i.e.* $y \propto x^\beta$ where (x, y) are the Cartesian coordinates of the outer boundary of the jet. Significantly, expansion is not described by $\beta = 1$, which would imply a constant

opening angle along the length of the jet until recollimation. Consequently it is hard to describe a given jet by a single opening angle. However, by measuring the opening angle from some fiducial point ($r = 145.4 r_j$) it was found that jets could be uniquely identified with respect to each other, as this value was observed to vary systematically with pressure and density. The regular expansion of the jets as shown by Jet 10 in Figure 15 is compelling evidence that this region might be described by an analytical expression in two dimensions derived from first principles, but such an expression is unspecified here. The development of such an expression would be a significant step towards understanding these jets, as much of what has been done in the past has been based on one-dimensional linear theory. The data collected in this project should provide a significant start in that direction.

4.3 Recollimation point

At the beginning of this project it was originally thought that recollimation occurred when the jet reached thermal pressure balance with the atmosphere. In fact the dynamics of the jet are dominated by ram pressure as the jet encounters the cocoon and the ambient medium. This is graphically demonstrated by the failure of the analytical jet model of Chapter 2, and the large amount of evidence compiled in Chapter 3.

In the region of parameter space explored, contours of the recollimation points (r_c) on a $p-\rho$ diagram were found to be given by power laws, as plotted in Figure 12 and compiled in Table 5. Original thinking implied that r_c was actually independent of density and uniquely dependent on the pressure of the jet. However, as Figure 12 shows, r_c is more dependent upon density than on pressure, which indicates that ram pressure is actually much more

significant in determining r_c than the thermal pressure of the jet. Here too, the potential for the discovery of an analytical expression that describes r_c as a function of pressure and density from first principles exists. Further study based on the results in this thesis should help in this respect.

4.4 General Comments

The HR simulation of § 3.2 produces a power output of $P_j = 3.6 \times 10^{36}$ W. This is ~ 4.5 times larger than the integrated intensity of the synchrotron emission of the M87 system, $P_T \sim 8 \times 10^{35}$ W. Since a counter-jet probably exists which delivers a similar amount of energy to the lobes, this implies an efficiency ϵ of converting P_j to electromagnetic radiation of ~ 0.1 . The HR simulation also produces a mass flux, $\dot{m} = 0.0143 M_\odot \text{ yr}^{-1}$, which is approximately two orders of magnitude lower than the observed mass accretion rates from the cooling flow onto the central SMBH. The values of P_j and \dot{m} provide a independent consistency check and show that the best density estimate for the M87 jet is plausible.

Future work to explore the parameter space containing the M87 initial conditions should include the effect of varying the velocity, instead of keeping it fixed at the ill-determined value of $0.3c$ as has been done here. Each value of velocity will have associated with it a dependence on r_c and θ_o as in Figure 12, each defining a unique point describing possible initial conditions for the M87 jet. In other words, a curve in v_j - p - ρ space will describe the initial conditions which reproduce the opening angle and recollimation point of the M87 jet. The addition of another variable will introduce another degree of freedom and may allow a third observational constraint (*e.g.* disruption point of the jet) to be accounted for in the

simulations.

Two important final conclusions should be extracted from this discussion. First, ram pressure effects dominate the morphology of the M87 jet, and presumably jets of similar type (a well-defined expansion, followed by recollimation). The ram pressure seems to dominate the position of recollimation, and perhaps is a significant contributor to the expansion rate of the jet. These effects were not appreciated in full at the beginning of this project. Second, given their age and the speed at which the simulations of Chapter 3 reached steady-state, jets of the M87 type have either reached steady-state (at least the inner regions), or are evolving but slowly at the present time.

Upon the collection of future observational data, the methods described in this project will allow for quick convergence of the new observational results and numerical simulations. This is particularly true if accompanying semi-analytical descriptions of the initial conditions on the opening angle and recollimation point can be developed from the data presented herein. The applicability of the method to other sources should allow other extragalactic jets to be modelled successfully, and significantly increase our knowledge and understanding of these complex objects.

References

- Appl, S, & Caminzind, M. 1992, *A&A*, **256**, 354
- Bertschinger, E., & Meiksin, A. 1986, *ApJ*, **306**, L1
- Bicknell, G. V. & Begelman, M. C. 1996 in *Energy Transport in Radio Galaxies and Quasars*, ed. P. E. Hardee, A. H. Bridle, & J. A. Zensus (San Francisco: Astronomical Society of the Pacific), p. 199
- Biretta, J. A. 1994 in *Astrophysical Jets*, ed. D. Burgarella, M. Livio, & C. P. O'Dea (Cambridge: Cambridge University Press), p. 263
- Biretta, J. A., Stern, C. P., & Harris, D. E. 1991, *AJ*, **101**, 1632
- Biretta, J. A., Zhou, F., & Owen, F. N. 1995, *ApJ*, **447**, 582
- Canizares, C. R., Clarke, G. W., Jernigan, J. G., & Markert, T. H. 1982, *ApJ*, **262**, 33
- Celotti, A., & Fabian, A. C. 1993, *MNRAS*, **264**, 228
- Chakrabarti, S. K. 1995, *ApJ*, **441**, 576
- Clarke, D. A. 1996a, *ApJ*, **457**, 291
- Clarke, D. A. 1996b in *Energy Transport in Radio Galaxies and Quasars*, ed. P. E. Hardee, A. H. Bridle, & J. A. Zensus (San Francisco: Astronomical Society of the Pacific), p. 311
- Clarke, D. A., Bridle, A. H., Burns, J. O., Perley, R. A., & Norman, M. L. 1992, *ApJ*, **385**, 173
- Clarke, D. A., Burns, J. O., & Norman, M. L. 1992, *ApJ*, **395**, 444

- Clarke, D. A., Harris, D. E., Carilli, C. L. 1996, *MNRAS*, submitted
- Clarke, D. A., Norman, M. L., & Burns, J. O. 1986, *ApJ*, **311**, L63
- Contopoulos, J., & Lovelace, R. V. E. 1994, *ApJ*, **429**, 139
- Curtis, H. D. 1918, *Pub. Lick Obs.*, **13**, 31
- Fabricant, D. & Gorenstein, P. 1983, *ApJ*, **267**, 535 (FG)
- Falle, S. A. E. G., & Wilson, M. J. 1985, *MNRAS*, **216**, 79
- Falle, S. A. E. G., & Wilson, M. J. 1986, *Can. J. Phys.*, **64**, 470
- Fanaroff, B. L., & Riley, J. M. 1974, *MNRAS*, **167**, 31P
- Ford, H. C., Harms, R. J., Tsvetanov, Z. I., Hartig, G. F., Dressel, L. L., Kriss, G. A.,
Bohlin, R. C., Davidsen, A. F., Margon, B., & Kochhar, A. J. 1994, *ApJ*, **435**, L27
- Ghisellini, G., Celotti, A., George, I. M., & Fabian, A. C. 1992, *MNRAS*, **258**, 776
- Harms, R. J., Ford, H. C., Tsvetanov, Z. I., Hartig, G. F., Dressel, L. L., Kriss, G. A.,
Bohlin, R. C., Davidsen, A. F., Margon, B., & Kochhar, A. J. 1994, *ApJ*, **435**, L35
- Hardee, P. E. 1982, *ApJ*, **257**, 509
- Hardee, P. E. 1986, *ApJ*, **303**, 111
- Hardee, P. E. 1987a, *ApJ*, **313**, 607
- Hardee, P. E. 1987b, *ApJ*, **318**, 78
- Hardee, P. E., Bridle, A. H., & Zensus, J. A. ed. 1996, *Energy Transport in Radio Galaxies
and Quasars* (San Francisco: Astronomical Society of the Pacific)
- Hardee, P. E., Clarke, D. A., & Howell, D. A. 1995, *ApJ*, **441**, 644

- Hardee, P. E., & Norman, M. L. 1988, *ApJ*, **334**, 70
- Hardee, P. E., & Norman, M. L. 1990, *ApJ*, **365**, 134
- Hardee, P. E., Norman, M. L., Koupelis, T., & Clarke, D. A. 1991, *ApJ*, **373**, 8
- Hardee, P. E., White, R. E., III, Norman, M. L. 1993 in *Jets in Extragalactic Radio Sources*,
ed. H.-J. Röser, K. Meisenheimer (Berlin: Springer-Verlag), p. 193 (HWN)
- Hardee, P. E., White, R. E., III, Norman, M. L., Cooper, M. A., & Clarke, D. A. 1992,
ApJ, **387**, 460
- Hesser, J. E., Harris, H. C., van den Bergh, S., Harris, G. L. H. 1984, *ApJ*, **276**, 491
- Hines, D. C., Owen, F. N., & Eilek, J. A. *ApJ*, **347**, 713,
- Jun, B.-I., Clarke, D. A., Norman, M. L. 1994, *ApJ*, **429**, 748
- Lea, S. M., Mushotzky, R., & Holt, S. S. 1982, *ApJ*, **262**, 24
- Lind, K. R., Payne, D. G., Meier, D. L., & Blandford, R. D. 1989, *ApJ*, **344**, 89
- Loken, C., Burns, J. O., & Clarke, D. A. 1993, *ApJ*, **417**, 515
- Neito, J.-L., & Lelievre, G. 1982, *A&A*, **109**, 95
- Neumann, M., Meisenheimer, K., Röser, H.-J., & Stickel, M. 1995, *A&A*, **296**, 662
- Norman, M. L., Winkler, K.-H. A., & Smarr, L. 1983 in *Astrophysical Jets*, ed. A. Ferrari
& A. G. Pacholzyk (Dordrecht: Reidel), p. 227
- Norman, M. L., Smarr, W., and Winkler, K.-H. A. 1985 in *Numerical Astrophysics*, ed.
J. M. Centrella, J. M. LeBlanc, & R. L. Bowers (Boston: Jones and Bartlett), p. 88
- Oppenheimer, B. R., & Biretta, J. A. 1994, *AJ*, **107**, 892

- Ouyed, R., Pudritz, R. E., Stone, J. M. 1996, preprint
- Owen, F. N., Hardee, P. E., & Cornwell, T. J. 1989, *ApJ*, **340**, 698 (OHC89)
- Peletier, R. F., & Jarvis, B. J. 1991, *A&A*, **247**, 315
- Reid, M. J., Biretta, J. A., Junor, W., Muxlow, T. W. B., & Spencer, R. E. 1989, *ApJ*, **336**, 112
- Reynolds, C. S., Fabian, A. C., Celotti, A., Rees, M. J. 1996, *MNRAS*, submitted
- Richtmyer, R. D., & Morton, K. W. 1967, *Difference Methods for Initial-Value Problems* (2d ed.; New York: Wiley Interscience)
- Sargent, W. L. W., Young, A. B., Boksenberg, A., Shortridge, K., Lynds, C. R., & Hartwick, F. D. A. 1978, *ApJ*, **221**, 831
- Sparks, W. B., Fraix-Burnet, D., Macchetto, F., & Owen, F. N. 1992, *Nature*, **355**, 804
- Spencer, R. E., & Junor, W. 1986, *Nature*, **321**, 753
- Stewart, G. C., Canizares, C. R., Fabian, A. C., & Nulsen, P. E. J. 1984, *ApJ*, **278**, 536
- Stiavelli, M., Biretta, J., Moller, P. & Zeilinger, W. W. 1992, *Nature*, **355**, 802
- Tsai, J. C. 1994a, *ApJ*, **423**, 143 (T94a)
- Tsai, J. C. 1994b, *ApJ*, **429**, 119 (T94b)
- Tucker, W. H., & Rosner, R. 1983, *ApJ*, **267**, 547 (TR)
- Turland, B. D. 1975, *MNRAS*, **170**, 281
- Ustyugova, G. V., Koldoba, A. V., Romanova, M. M., Chechetkin, V. M., Lovelace, R. V. E. 1995, *ApJ*, **439**, 39

van Leer, B. 1977, *J. Comp. Phys.*, **23**, 276

White, R. E. , III, & Sarazin, C. L. 1988, *ApJ*, **335**, 688

Curriculum Vitae

Michael Patrick Casey

Department of Astronomy
University of Toronto
Toronto, Ontario M5S 3H8
CANADA

Phone: (416) 978-3148(office)
(416) 709-3919(home)
Fax: (416) 971-2026
Email: casey@astro.utoronto.ca
WWW: <http://www.astro.utoronto.ca/casey>

Born: February 16, 1970
Halifax, Nova Scotia, Canada

Education:

Ph.D., Astronomy, University of Toronto, 1999 (projected).
M.Sc., Astronomy, Saint Mary's University, 1996.
B.Sc. Honours, Physics, Dalhousie University, 1993.

M.Sc. Thesis:

Title: Numerical Simulations of the Extragalactic Jet in M87
Advisor: Dr. David Clarke
Department of Astronomy and Physics, Saint Mary's University.

Work Experience:

Sept. 1989 - May 1990 Physics Department, Dalhousie University.
Sept. 1991 - Apr. 1994
Teaching assistant and/or lab demonstrator for various first year physics lecture and laboratory courses.

Summer 1993 Physics Department, Dalhousie University
Summer Research Assistant. Computer programming and data reduction work in support of the research lab of Dr. Daniel Labrie.

Summer 1994 Physics Department, Dalhousie University

Summer Laboratory Technician. Preparation of undergraduate physics laboratories for the upcoming 94/95 school year, particularly upper-year undergraduate laboratories. Work also included tests of new experiments and equipment introduced into the labs in the next term.

Sept. 1994 – Aug. 1996 Astronomy and Physics Department, Saint Mary's University

Research work for Master's thesis. The MHD computer code ZEUS-3D was used to simulate the extragalactic jet in M87 in two dimensions.

Teaching Assistant, 1st year physics courses (lab demonstrating and marking). Dr. Michael West's first year physics course was also taught for a week while he was away conducting research.

Conducted public tours for the Burke-Gaffney Observatory at Saint Mary's University approximately twice a term (weather permitting).

Awards and Fellowships:

1988	Dr. David M. Soloan Scholarship (Dalhousie entrance scholarship)
1994 – 1996	Saint Mary's Graduate Scholarship
1996 –	University of Toronto Open Doctoral Fellowship
1996 –	Carl Reinhardt Fellowship in Astronomy (University of Toronto)

Poster Papers:

Casey, M. P. & Clarke, D. A. 1996, "2D Hydrodynamical Calculations of the Jet in M87", *JRASC*, **90**, ??